Effect of Soil-Structure Interaction on Nonlinear Dynamic Response of Reinforced Concrete Structures

Mourlas, Christos; Khabele, Neo; Bark, Hussein A.; Karamitros, Dimitris; Taddei, Francesca; Markou, George

Published in:
International Journal of Structural Stability and Dynamics

DOI:
10.1142/S0219455420410138

Publication date:
2020

Document Version
Peer reviewed version

THE EFFECT OF SOIL-STRUCTURE INTERACTION ON THE NONLINEAR DYNAMIC RESPONSE OF REINFORCED CONCRETE STRUCTURES

Christos Mourlas[1], Neo Khabele[2], Hussein A. Bark[3], Dimitris Karamitros[4], Francesca Taddei[3], George Markou[2] and Manolis Papadrakakis[1]

[1] Institute of Structural Analysis & Seismic Research, National Technical University of Athens, 9 Iroon Polytechniou Str., Zografou Campus, GR-15780 Athens, Greece
e-mail: {mourlasch, mpapadra}@central.ntua.gr

[2] Department of Civil Engineering, University of Pretoria, South Africa
e-mail: u14030242@tuks.co.za; george.markou@up.ac.za

[3] Chair of Structural Mechanics, Technical University of Munich, Arcisstr. 21, 80333 Munich, Germany
e-mail: francesca.taddei@tum.de; hsein.bark@tum.de

[4] Department of Civil Engineering, University of Bristol Queen's Building, University Walk, Bristol BS8 1TR, United Kingdom
e-mail: d.karamitros@bristol.ac.uk

Abstract

Investigating the nonlinear dynamic response of reinforced concrete (RC) structures is of significant importance in understanding the expected behaviour of these structures under dynamic loading. This becomes more crucial during the design of new or the assessment of existing RC structures that are located in seismically active areas. The numerical simulation of this problem through the use of detailed 3D modelling is still a subject that has not been investigated thoroughly due to the significant challenges related to numerical instabilities and excessive computational demand, especially when the soil-structure interaction (SSI) phenomenon is accounted for. This work aims at presenting a nonlinear simulation tool to investigate this numerically cumbersome problem in order to provide further inside into the SSI effect on RC structures under nonlinear dynamic loading conditions. A detailed 3D numerical model of full-scale RC structures considering the SSI effect through modeling the nonlinear frame and soil domain, is performed and discussed herein. The constructed models are subjected to dynamic loading conditions and an elaborate investigation is presented considering different type of structures, material properties of soil domains and depths. The RC structures and the soil domains are modelled through 8-noded hexahedral isoparametric elements, where the steel bar reinforcement of concrete is modelled as embedded beam and truss finite elements. The Ramberg-Osgood constitutive law was used for modelling the soil domain. It was shown that the SSI effect can significantly increase the flexibility of the system, altering the nonlinear dynamic response of the RC frames causing local damages that are not observed when the fixed-base model is analysed. Furthermore, it was found that the structures founded on soft soil developed larger base-shear compared to the fixed-base model which is attributed to resonance phenomena connected to the SSI effect and the imposed accelerograms.

Keywords: Nonlinear Dynamic Analysis, Soil-Structure Interaction, Reinforced Concrete Structures, Seismic Assessment, Stability of Structures

1. Introduction

A number of researchers have studied the influence of soil-structure interaction (SSI) on the seismic behaviour of structures during the last decades. However, it is still very

common to analyse the response of a fixed-base structure by neglecting the SSI effect. In some cases, codes provide with seismic design provisions that consider the SSI effect, by reducing the base shear of the fixed-base structures, where in others they suggest to perform advanced analysis for investigating the overall effect (ASCE [1], NEHRP [2]). These provisions are based on linear, viscously damped, structures that are subjected to transient or steady-state excitations (Bielak [3], Jennings and Bielak [4], Veletsos and Meek [5], Luco [6] and Roesset [7]). Nevertheless, the effect of the inelastic behaviour of soil on the inelastic dynamic behaviour of the structure has not been completely addressed in the literature. It is evident that the role of the SSI in structural seismic performance (Mylonakis and Gazetas [8]) is a research subject that raise a lot of controversy among the researchers.

There are several papers that investigate and stress the necessity of nonlinear analysis in order to determine the effect of SSI on buildings [9-11]. One of these research works is found in [12], where a plain strain numerical study indicated that in saturated soil-conditions the dynamic SSI is negligible but on dry soil cases the results are inconsistent. Veletsos and Verbic [13], investigated the response of single-story elastoplastic structures supported to an elastic half-space subjected to a simple pulse loading type. It was concluded that the increase of the yielding of the structure would increase the flexibility of the system, which led to the decrease of the SSI effect. However, Bielak [14] investigated the steady-state response of a bilinear hysteretic structure supported on an elastic half-space and found that, contrary to the response of the linear systems, the resonant amplitude of the response considering SSI effects, could be larger than that derived by a structure with a rigid foundation. This finding has been supported by several studies [15-18].

Many researchers have concluded that a realistic modelling approach can lead to different seismic design recommendations in cases of flexible soil foundations [12]. In [18], it is demonstrated that the flexible foundation will increase its natural period compared to the fixed-base model and cause the energy dissipation of the system to increase. The increase of the period will result to an increase of the seismic coefficient on an ascending branch of the response spectrum and a respective decrease in the descending branch. Additionally, the increase of the energy dissipation will tend to decrease the spectral ordinate. Furthermore, as it is described in [19], the current seismic design codes cannot be used in cases where flexible-base structures with SSI effects occur. In this article [19], the effect of SSI on seismic performance of multi-storey buildings was investigated and was found that the SSI can reduce the strength and ductility demand of the buildings up to 60% in comparison to the fixed-base structure. Finally, a study by Tomeo et al. [20], showed that considering the SSI on 2D RC moment resisting frames, the inter-storey drift ratio and the maximum base shear can be reduced up to 50% and 20%, respectively in comparison to the fixed-base model.

Multiple models that have been developed to study the SSI effect rely on simplistic approximations that foresee the use of beam-column finite elements for the discretization of the superstructure, while the soil domain is modelled through springs of 2D finite elements. Most of the models found in the international literature use simple single-degree-of freedom structures [21], 2D numerical simulation, and shear-building models [22, 23] for the substructure. The SSI effect can be modelled through the use of the substructure and the direct method [24-27], which are well-known simulation approaches. Furthermore, in order to reduce the computational cost, springs (Winkler-based approaches) and dashpots are commonly used to describe the behaviour of the soil. Alternatively, simple cone models [28-30] are implemented to simulate the soil interaction, whereas, equivalent linear methods [31-33] have been proposed in order to

simulate the non-linear effects within the soil domain. The Beam-on-Nonlinear-Winkler Foundation numerical model [20, 34] has been also used to model the effect of the nonlinear foundation, which is characterized by its simplicity and minimum computational cost. Finally, several studies have developed dynamic macroelements [35-39] considering SSI effects typically within a single element and using a plasticity-based formulation for the superstructure found on shallow foundations.

A number of studies have used 2D quadrilateral finite elements for the soil domain [40-42], as well as the much more computationally demanding, but more accurate, 3D numerical models [12, 43-47].

This research work aims to shed light on the controversy whether the consideration or the negligence of the SSI effect is on the side of safety or not for the dynamic assessment of RC structures through 3D detailed nonlinear numerical analysis. To achieve this objective, the SSI effect is investigated by considering the nonlinear behaviour in both soil and superstructure, using 3D numerical modelling approaches. The material of concrete is modelled through the constitutive model proposed in [48-52], which is based on the Kotsovos and Pavlovic [53] material model, while for the soil, the Ramberg-Osgood [54] model is implemented. The results of this investigation indicate that although the soil increases the flexibility of the soil-structure system, it decreases the fundamental frequency which can lead to resonance effects. These effects can be present when the fundamental frequency of the system reaches the frequency of the peak of excitation or the eigenfrequency of the soil [55].

In this research work, a 2-storey RC test frame specimen was used to develop the presented numerical investigation of the SSI effects. The RC frame that was tested at a seismic table [56] was one of the models used to validate the developed algorithm [50] in capturing the nonlinear dynamic response of RC structures. The developed simulation tool for the needs of this research work was integrated within the software code Reconan FEA [60]. In addition to the 2-storey RC test frame, a four-column 2-storey RC building was analysed under dynamic loading conditions. Different soil properties and depths have been investigated, and compared with the nonlinear dynamic behaviour of fixed-base models, in order to demonstrate the nature and level of the SSI effect. Both superstructure and soil domain are discretized through the use of 8-noded hexahedral elements, while the steel bars are modelled as embedded rebars, in an attempt to achieve that maximum discretization accuracy during the nonlinear dynamic analysis.

2. Constitutive Material Modelling

2.1 Concrete material model

The concrete was represented using the constitutive model described in [48-50] and it is based on an experimental study of Kotsovos and Pavlovic [53] and a numerical modelling approach presented in [50]. The model describes realistically the triaxial behaviour of concrete using as input parameters only the Young modulus, the Poisson ratio and the uniaxial compressive strength of concrete. The tensile strength of concrete is set to be 10% of the uniaxial compressive strength and the other damage parameters that describe the nonlinear cyclic and dynamic behaviour are defined based on the recommendations found in [50].

The concrete material model is mathematically formulated with the hydrostatic (σ_0) and deviatoric (τ_0) components, the bulk (K) and shear (G) modulus of elasticity and an external stress (σ_{id}). The stress-strain relations can take the following form:

$$\varepsilon_0 = \varepsilon_{0(h)} + \varepsilon_{0(d)} = (\sigma_0 + \sigma_{id}) / (3K_s) \quad (1)$$

$$\gamma_0 = \gamma_{0(d)} = \tau_0 / (2G_s) \tag{2}$$

where, (σ_0, τ_0) are the normal and shear octahedral stresses and (ε_0, γ_0) are the normal and shear octahedral strains. The K_s and G_s are the secant forms of bulk and shear moduli, which describe the non-linear σ_0-$\varepsilon_{0(h)}$ and τ_0-$\gamma_{0(d)}$ relations, respectively (h and d refer to the hydrostatic and deviatoric components, respectively). The σ_{id} represents the coupling relation of τ_0-$\varepsilon_{0(d)}$. The stress-strain relationship of the uncracked concrete Gauss Point (GP) is given by:

$$\begin{bmatrix} \sigma_x \\ \sigma_y \\ \sigma_z \\ \sigma_{xy} \\ \sigma_{xz} \\ \sigma_{yz} \end{bmatrix} = \begin{bmatrix} 2G_t+\mu & \mu & \mu & 0 & 0 & 0 \\ \mu & 2G_t+\mu & \mu & 0 & 0 & 0 \\ \mu & \mu & 2G_t+\mu & 0 & 0 & 0 \\ 0 & 0 & 0 & G_t & 0 & 0 \\ 0 & 0 & 0 & 0 & G_t & 0 \\ 0 & 0 & 0 & 0 & 0 & G_t \end{bmatrix} \cdot \begin{bmatrix} \varepsilon_x \\ \varepsilon_y \\ \varepsilon_z \\ \varepsilon_{xy} \\ \varepsilon_{xz} \\ \varepsilon_{yz} \end{bmatrix} \tag{3}$$

where $\mu = K_t - 2\,G_t/3$. It was found in [53] that when the deviatoric stress exceeds 50% of the ultimate strength, then the parameters $K_t=K_t(\sigma_0,\tau_0,f_c)$ and $G_t=G_t(\sigma_0,\tau_0,f_c)$ are updated through their analytical expressions provided in [53], while an elastic material response is considered when the deviatoric stress is less than 50% of the ultimate strength of concrete.

The ultimate strength of concrete is expressed in terms of the deviatoric stress through the Willam and Warkne [57] envelope:

$$\tau_{0u} = \frac{2\tau_{0c}(\tau_{0c}^2 - \tau_{0e}^2)\cos\theta + \tau_{0c}(2\tau_{0e} - \tau_{0c})\sqrt{4(\tau_{0c}^2 - \tau_{0e}^2)\cos^2\theta + 5\tau_{0e}^2 - 4\tau_{0c}^2\tau_{0e}^2}}{4(\tau_{0c}^2 - \tau_{0e}^2)\cos^2\theta + (2\tau_{0e} - \tau_{0c})^2} \tag{4}$$

where θ is the angle that defines the deviatoric stress orientation on the octahedral plane. Additionally, the $\tau_{0e}(f_c,\sigma_0)$ and $\tau_{0c}(f_c,\sigma_0)$ are defined by analytical expressions that are found in [53] and correspond to $\theta=0°$ ($\sigma_1=\sigma_2>\sigma_3$-triaxial extension) and $\theta=60°$ ($\sigma_1>\sigma_2=\sigma_3$ -triaxial compression), respectively.

The concrete cracking is modelled through the adoption of the smeared crack approach. When the deviatoric stress in a GP exceeds the above ultimate deviatoric strength (τ_{0u} in Eq. 4), then a crack opens and the stiffness that corresponds to the direction of the maximum principle stress is set to zero. Therefore, the constitutive matrix in the crack plane (local system assuming that the crack is perpendicular to z' axis, see Fig.1) is given by:

$$C_l = \begin{bmatrix} 2G_t+\mu & \mu & 0 & 0 & 0 & 0 \\ \mu & 2G_t+\mu & 0 & 0 & 0 & 0 \\ 0 & 0 & 0 & 0 & 0 & 0 \\ 0 & 0 & 0 & G_t & 0 & 0 \\ 0 & 0 & 0 & 0 & \beta G_t & 0 \\ 0 & 0 & 0 & 0 & 0 & \beta G_t \end{bmatrix} \tag{5}$$

where β is a shear retention factor [49] which is set to β=0.05. The stresses and the constitutive matrix in the global coordinate system are calculated through the use of the following expression:

$$\boldsymbol{\sigma}_{\mathrm{Cr}} = \boldsymbol{T}^{-1}\left[\sigma_1 = 0 \quad \sigma_2 \quad \sigma_3 \quad 0 \quad 0 \quad 0\right]^{\mathrm{T}} \tag{6}$$

$$\boldsymbol{C}_{gl} = \boldsymbol{T}^T \boldsymbol{C}_l \boldsymbol{T} \tag{7}$$

where $\boldsymbol{T}$ is the transformation matrix that transforms the principal stress axes (x', y', z') to the initial x, y and z axes with the use of the direction cosines (l_i, m_i, n_i) and it is given by:

$$\boldsymbol{T} = \begin{bmatrix} l_1^2 & m_1^2 & n_1^2 & l_1 m_1 & m_1 n_1 & n_1 l_1 \\ l_2^2 & m_2^2 & n_2^2 & l_2 m_2 & m_2 n_2 & n_2 l_2 \\ l_3^2 & m_3^2 & n_3^2 & l_3 m_3 & m_3 n_3 & n_3 l_3 \\ 2l_1 l_2 & 2m_1 m_2 & 2n_1 n_2 & l_1 m_2 + l_2 m_1 & m_1 n_2 + m_2 n_1 & n_1 l_2 + n_2 l_1 \\ 2l_3 l_1 & 2m_3 m_1 & 2n_3 n_1 & l_3 m_1 + l_1 m_3 & m_3 n_1 + m_1 n_3 & n_3 l_1 + n_1 l_3 \\ 2l_2 l_3 & 2m_2 m_3 & 2n_2 n_3 & l_2 m_3 + l_3 m_2 & m_2 n_3 + m_3 n_2 & n_2 l_3 + n_3 l_2 \end{bmatrix} \tag{8}$$

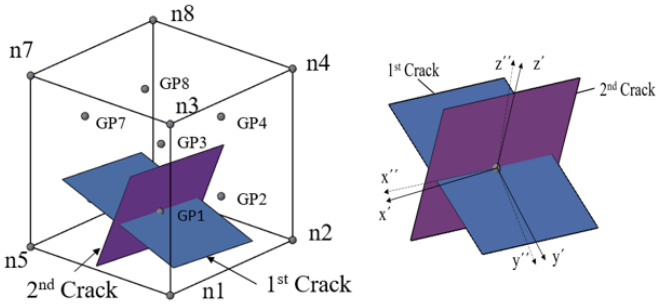

Fig. 1. Local axes for the case of two cracks at a specific Gauss point. [51]

The same procedure is followed in order to calculate the stresses and the constitutive matrix for the case of two and three cracks as described in [50]. During cyclic and dynamic loading conditions, the pre-existing cracks will tend to close due to load reversals. This phenomenon is captured numerically by the assumption that the cracks are closing as the strains vertical to crack planes are becoming small enough. In [49] it was found that, the criterion of crack closure can be expressed in the following form:

$$\varepsilon_i \leq a \cdot \varepsilon_{cr} \tag{9}$$

where ε_i is the current strain in the i-direction which is normal to the crack plane and ε_{cr} is the strain that caused the crack formation. Parameter a is a reduction factor, which takes the following form:

$$a = 1 - \frac{\varepsilon_{cr}}{\varepsilon_{\max}} = \frac{\varepsilon_{\max} - \varepsilon_{cr}}{\varepsilon_{\max}} \tag{10}$$

The maximum strain ε_{max} is re-defined through the nonlinear Newton-Raphson iterative procedure. When the criterion of failure is satisfied, the crack is assumed that it is closed and the restoring stiffness along the previous crack planes is a part of the initial uncracked stiffness of concrete. Assuming that the criterion of failure is satisfied in a Gauss point (GP) with one crack (Eq. 5), then the new constitutive matrix is given through the following expression:

$$\boldsymbol{C}_t = \begin{bmatrix} 2G_t + \mu & \mu & a_n \cdot (1 - D_c) \cdot \mu & 0 & 0 & 0 \\ \mu & 2G_t + \mu & a_n \cdot (1 - D_c) \cdot \mu & 0 & 0 & 0 \\ a_n \cdot (1 - D_c) \cdot \mu & a_n \cdot (1 - D_c) \cdot \mu & a_n \cdot (1 - D_c) \cdot (2G_t + \mu) & 0 & 0 & 0 \\ 0 & 0 & 0 & a_s \cdot (1 - D_c) \cdot \beta \cdot G_t & 0 & 0 \\ 0 & 0 & 0 & 0 & a_s \cdot (1 - D_c) \cdot \beta \cdot G_t & 0 \\ 0 & 0 & 0 & 0 & 0 & a_s \cdot (1 - D_c) \cdot \beta \cdot G_t \end{bmatrix} \tag{11}$$

where a_n and a_s are constants with recommended values [50] of 0.25 and 0.125,

respectively. The concrete damage factor D_c is defined by the following equation:

$$D_c = e^{-(1-a)/f_{cc}} = e^{-\left(1-\left(1-\frac{\varepsilon_{cr}}{\varepsilon_{\max}}\right)\right)/f_{cc}} = e^{-\left(\frac{\varepsilon_{cr}}{\varepsilon_{\max}}\right)/f_{cc}} \tag{12}$$

where f_{cc} measures the number of times that a crack has closed and it is re-calculated at every Newton-Raphson iteration for each GP. More details about this constitutive modelling approach can be found in [50]. The schematic representation of the constitutive model is depicted in Fig. 2.

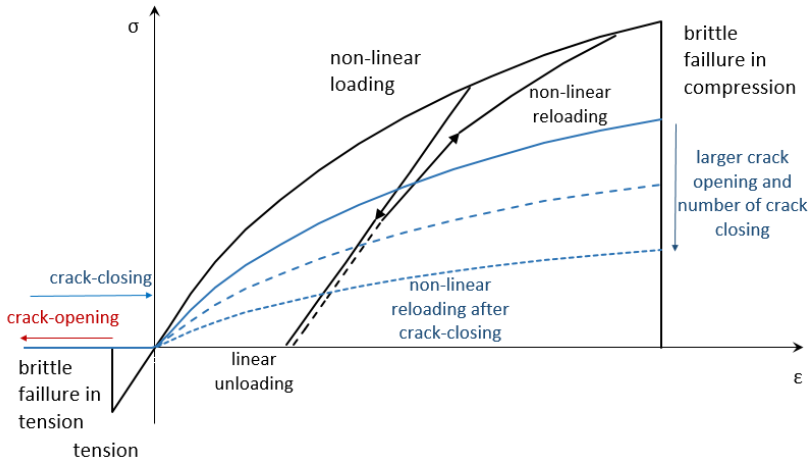

Figure 2. Schematic representation of the stress-strain relationship for the behaviour of concrete under cyclic loading conditions.

2.2 Steel Reinforcement material model

The Menegotto-Pinto [58] model is used to model the steel reinforcement behaviour. The model takes into account the accumulated material deterioration due to crack opening/closure that has been gathered at each GP found around the embedded rebar element. Due to this phenomenon, a reduction factor has been introduced in [50] that represents the loss of bonding between steel reinforcement and the surrounding damaged (cracked) concrete. The damage factor reduces the Young modulus of elasticity of the material through the use of the following equation:

$$E_s^{'} = (1-D_s)E_s \tag{13}$$

where

$$D_s = \left[1-a_{Element}\right] \tag{14}$$

$$a_{Element} = \frac{\sum_{1}^{ncr} a_i}{ncr} \text{ and } ncr \text{ is the number of cracked Gauss Points} \tag{15}$$

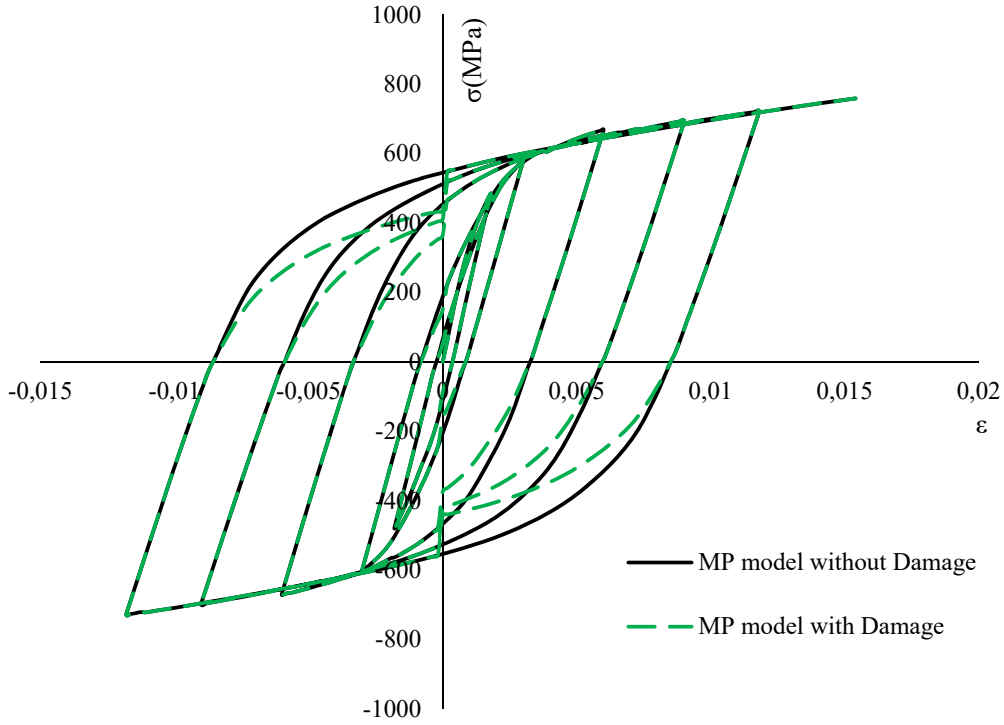

Figure 3. Menegotto-Pinto steel model that accounts for the accumulated damage due to the opening and closure of cracks.

The material deterioration is implemented when $\sigma_s \cdot \varepsilon_s < 0$, in order to represent the pinching phenomena that appears during the cyclic analysis due to loss of bonding of the steel rebars when crack opening/closure takes place. The constitutive stress-strain relation of the Menegotto-Pinto material model with the proposed steel damage factor is illustrated in Fig. 3.

2.3 Soil model

The behaviour of soil is described by the one-dimensional hysteretic model of Ramberg and Osgood model [54]. This well-established numerical material model can effectively simulate the degradation of shear modulus in soils and the corresponding increase of viscous damping with increasing shear strain amplitude. The shear stress-strain is given by the following equation:

$$\gamma = \frac{\tau}{G} + \kappa \left(\frac{\tau}{G} \right)^k \tag{16}$$

where G is the maximum shear modulus (G_{max}) and (κ, k) are model parameters. Parameter κ can be substituted by a variable α_1 as follows:

$$a_1 = \frac{\tau_1}{G\gamma_1} \Leftrightarrow \gamma_1 = \frac{\tau_1}{G\alpha_1} = \frac{\tau_1}{G} + \kappa \left(\frac{\tau_1}{G\gamma_1} \right)^k \tag{17}$$

where γ_1 is a characteristic strain which is also an input parameter and corresponds to the shear stress τ_1 which can be defined by Eq. 17. Therefore, κ can be expressed by the following equation:

$$\kappa = \left(\frac{1}{\alpha_1} - 1\right)\left(\frac{G}{\tau_1}\right)^{k-1} \tag{18}$$

Eq. 16 can be written as:

$$\gamma = \frac{\tau}{G} + \left(\frac{1}{\alpha_1} - 1\right)\frac{\tau}{G}\left(\frac{\tau}{\tau_1}\right)^{k-1} \tag{19}$$

The secant G_s and tangent G_t and the shear modulus are related to the maximum shear modulus G_{max} as:

$$\begin{aligned} G_s(\tau) &= \frac{G_{max}}{T_s(\tau)} = \frac{G_{max}}{1 + \left(\frac{1}{a_1} - 1\right)\left(\frac{\tau}{\tau_1}\right)^{k-1}} \\ G_t(\tau) &= \frac{G_{max}}{T_t(\tau)} = \frac{G_{max}}{1 + k\left(\frac{1}{a_1} - 1\right)\left(\frac{\tau}{\tau_1}\right)^{k-1}} \end{aligned} \tag{20}$$

where T is a positive scalar greater than 1 that expresses the reduction of elastic shear modulus. After the first load reversal, τ_1 in the above expressions is substituted by $2\tau_1$ to satisfy the Masing rules [59]. Therefore, the expression for the T_s becomes:

$$T_s(\tau) = \begin{cases} 1 + \left(\frac{1}{a_1} - 1\right)\left(\frac{\tau}{\tau_1}\right)^{k-1} & \text{at first loading} \\ 1 + \left(\frac{1}{a_1} - 1\right)\left(\frac{\tau}{2\tau_1}\right)^{k-1} & \text{after load reversal} \end{cases} \tag{21}$$

Under multiaxial stress-state, the secant constitutive material matrix can be defined by the following expression:

$$C_s = \frac{1}{T_s}\begin{bmatrix} K + \frac{4}{3}G & K - \frac{4}{3}G & K - \frac{4}{3}G & 0 & 0 & 0 \\ K - \frac{4}{3}G & K + \frac{4}{3}G & K - \frac{4}{3}G & 0 & 0 & 0 \\ K - \frac{4}{3}G & K - \frac{4}{3}G & K + \frac{4}{3}G & 0 & 0 & 0 \\ 0 & 0 & 0 & 2G & 0 & 0 \\ 0 & 0 & 0 & 0 & 2G & 0 \\ 0 & 0 & 0 & 0 & 0 & 2G \end{bmatrix} \tag{22}$$

where K is the bulk modulus. This expression implies that the Poisson's ratio ν is constant so that:

$$\frac{G}{K} = \frac{G_s}{K_s} = \frac{G_t}{K_t} = \frac{3(1-2\nu)}{2(1+\nu)} \tag{23}$$

The schematic representation of the Ramberg-Osgood model with tangent and secant

constitutive material matrix, is illustrated in Fig. 4.

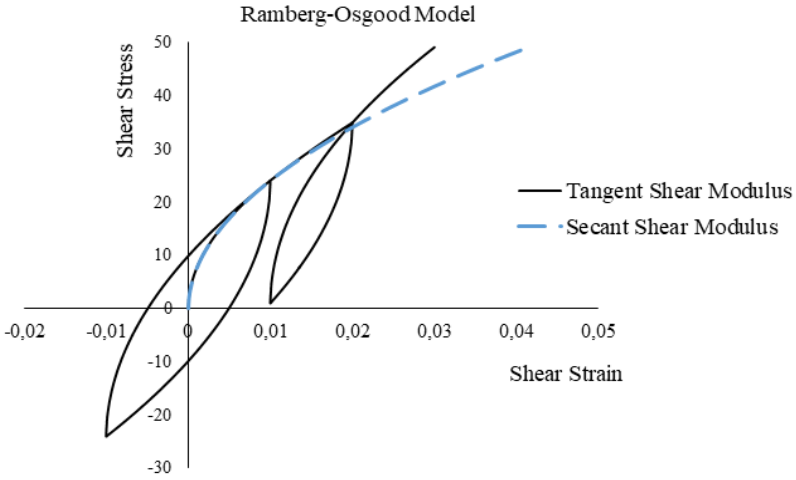

Figure 4. Hysteretic model by Ramberg-Osgood equations with tangent and secant shear modulus.

2.4 Additional Validation

As it was presented in [50] and [60], Reconan FEA code [61] has the ability to predict the nonlinear dynamic behaviour of RC structures and capture the soil mechanical behaviour under different loading conditions. Furthermore, the software was successfully used to capture the mechanical behaviour of a RC 6-pile foundation system embedded in soil [62] that was tested under ultimate limit state conditions. Further validation is performed herein through the use of formulae found in the international literature [63] that predict the expected soil settlement under an isolated footing.

The RC structure shown in Fig. 4 has a height of 7.5 m and a width of 4.5 m, where the width and length of the soil domain was 3 times the corresponding dimensions of the RC frame. The columns have a square section (30x30 cm^2) with an isolated footing with dimensions of 1.2x1.2 m^2. The shear wall has a section of 30x150 cm^2, where it is founded on a footing with dimensions of 1.2x2.4 m^2. The depth of the soil mesh was set to be equal to 10 m. The material properties used to construct the numerical model in Fig. 4 and to compute the settlement analytically are shown in Table 1.

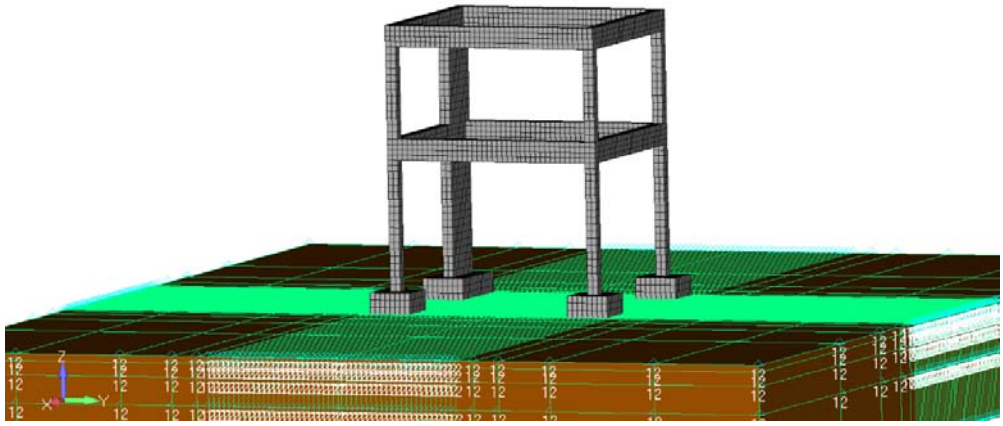

Figure 5. RC frame founded on isolated footings with service loads.

RC Density ρ (kN/m^3)	Soil Young's Modulus E (MPa)	Soil Ultimate Stress $f_{u,soil}$ (kPa)	Numerically obtained Vertical Stress σ (kPa)	Volume Compressibility [65] m_v (MPa^{-1})	Poisson's ratio v
25	70	900	380	0.9	0.3

Table 1. Soil material properties used for the validation process

The model in Fig. 5 was used to estimate the settlement due to the self-weight of the 2-storey RC frame, and compare it to the analytic equations currently utilised in practise for settlement calculation, which can be found in [63]. The settlement can be computed through the following expression:

$$s = \sigma \cdot H \cdot m_v \tag{24}$$

where, s is the total settlement, σ is the total applied vertical stress in kPa, H is the soil depth and m_v the coefficient of volume compressibility. The value of m_v is assumed to be equal to 0.9 MPa^{-1} which corresponds to an acceptable value of a highly compressible clay material [64].

The total applied load was divided into two load increments. Based on the analysis, the soil domain remained in the elastic region thus the maximum vertical stress σ shown in Table 1 was small enough to maintain a linear behaviour. The obtained settlement under the smaller footings was found equal to 1.18 mm, where Eq. 24 gave a 1.33 mm settlement. Furthermore, for load increment 2, a total of 2.36 mm compared to the 2.66 mm obtained from the analytical formula. The differences between the two methods are attributed to the simplicity of the analytical formula that does not take into consideration 3D stress state phenomena, which take place when the soil domain is compressed. Most importantly, the volume compressibility parameter of soil was not obtained from experimental testing, but was assumed based on the characteristics of the soil at hand. Therefore, there is an evident advantage when implementing 3D FEM when investigating this type of mechanical problems.

3. Dynamic Nonlinear Analysis

For the solution of the equation of motion in dynamic analysis, the Newmark method has been implemented. This implicit integration method is suitable in earthquake analysis, because it is characterized by an acceptable numerical stability even for nonlinear structural response. Thus, the time step does not have to be very small that could increase the computational cost of the analysis. Therefore, the equilibrium of the system at time $t+\Delta t$ is given by the following expression:

$$ {}^{t}\hat{\boldsymbol{K}}\Delta\boldsymbol{U}^{(k)} = {}^{t+\Delta t}\boldsymbol{R} - {}^{t+\Delta t}\boldsymbol{F}^{(k-1)} - \boldsymbol{M}\left(\frac{4}{\Delta t^2}\left({}^{t+\Delta t}\boldsymbol{U}^{(k-1)} - {}^{t}\boldsymbol{U}\right) - \frac{4}{\Delta t}{}^{t}\dot{\boldsymbol{U}} - {}^{t}\ddot{\boldsymbol{U}}\right) - \boldsymbol{C}\left(\frac{2}{\Delta t}\left({}^{t+\Delta t}\boldsymbol{U}^{(k-1)} - {}^{t}\boldsymbol{U}\right)\right. \tag{25}$$

where $\boldsymbol{U}$,$\dot{\boldsymbol{U}}$ and $\ddot{\boldsymbol{U}}$ are the vector of displacements, velocity and acceleration of the system, respectively. $\boldsymbol{R}$ is the external applied load vector, $\boldsymbol{F}$ is the internal load vector equivalent to the element stresses, $\boldsymbol{M}$ is the mass matrix, $\boldsymbol{C}$ is the damping matrix and k is the Newton Raphson iteration. The matrix ${}^{t}\hat{\boldsymbol{K}}$ is given by:

$$ {}^{t}\hat{\boldsymbol{K}} = {}^{t}\boldsymbol{K} + \frac{4}{\Delta t^2}\boldsymbol{M} + \frac{2}{\Delta t}\boldsymbol{C} \tag{26}$$

where ${}^{t}\boldsymbol{K}$ is the tangent stiffness matrix of the system.

For the investigated models, the lumped diagonal matrix has been used, where the Rayleigh damping known as proportional damping was used for the damping matrix

expression found in Eq. 27.

$$\boldsymbol{C} = a_K \cdot \boldsymbol{K} + a_M \cdot \boldsymbol{M} \tag{27}$$

$$a_K = \frac{2 \cdot \xi}{\omega_1 + \omega_2},\ a_M = \frac{2 \cdot \xi \cdot \omega_1 \cdot \omega_2}{\omega_1 + \omega_2} \tag{28}$$

where, ξ is the damping ratio and the ω_1, ω_2 are the first (minimum) angular frequencies of the system. It has to be noted, that the damping ratio matrix **C** for the case of the soil domain was assumed to participate only for the computation of the stiffness matrix in Eq. 26, therefore, the contribution of the soil to the Rayleigh damping matrix, is calculated by Eq. 27 with $\boldsymbol{M}$ = 0. This assumption was adopted to avoid including excessive damping in the numerical model due to the large soil domain and allow the SSI phenomena to develop without any artificial numerical limitations, such as the energy dissipation that occurs due to the assumed damping ratio.

The eigenfrequencies and the eigenvalues are calculated by conducting modal analysis using the subspace iteration procedure described in detail in [65]. The Newton-Raphson iterative method that is used for the analyses performed in this study, implements an energy convergence tolerance criterion with a convergence tolerance set to 10^{-4}.

4. Numerical investigation of SSI

4.1. Two-storey RC Frame

In [50] the nonlinear dynamic behaviour of two-storey RC frames was numerically investigated. These two-storey frames were designed and experimentally investigated according to Eurocode provisions for the design of earthquake-resistant structures by Carydis [56]. Particularly, the RC frame H30 shown in Fig. 6 was designed to exhibit a higher ductility (q = 5). The masses of the specimen were 2.87 and 2.62 tons, which were applied at the lower and upper storeys, respectively. The uniaxial compressive strength of concrete (f_c) was 50 MPa and the yielding stress (f_y) of the steel reinforcement was 500 MPa.

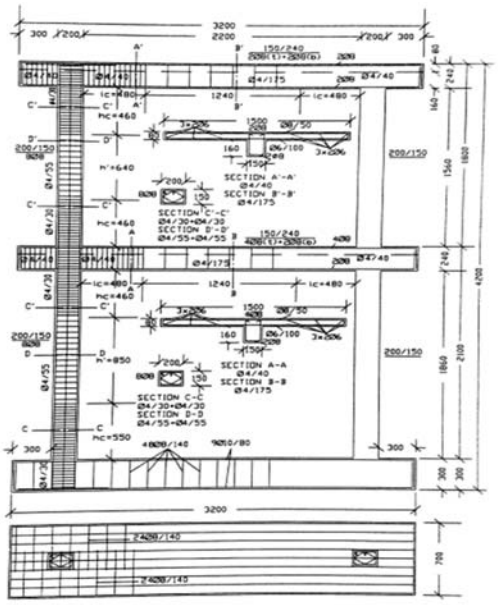

Figure 6. Geometric and reinforcement details of the RC-frame specimen H30. [56]

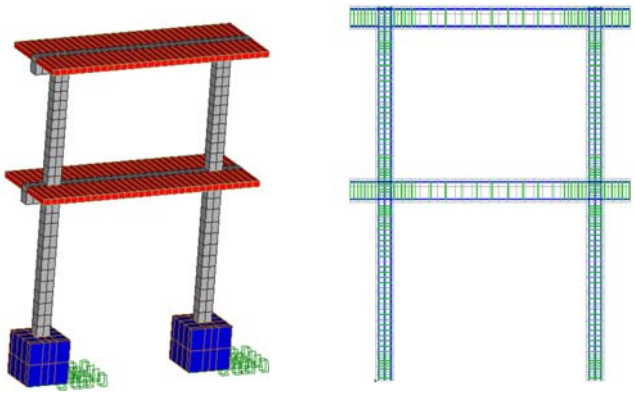

Figure 7. 3D view of the FE mesh of 8-noded hexahedral and embedded rebar elements (H30 model [50])

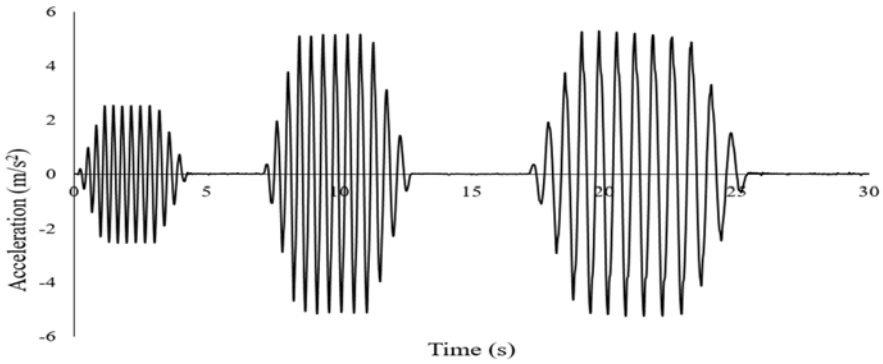

Figure 8. Base acceleration that were subjected during the experiments [56] and the numerical analyses of specimen H30.

The concrete domain is discretized by 224 hexahedral finite elements (10cm x 15cm x 15.5cm) and the steel bars were modelled through the use of 2,384 steel embedded beam elements as shown in Fig 7. Furthermore, 128 8-noded hexahedral elements were used (red elements in Fig. 7) for the discretization of the RC slabs. All the displacements of the RC structure (fixed and SSI) that are calculated are relevant displacements of the masses (plates) to the base of the structure.

The sine-like acceleration records applied at the base of the structure along the plane of the frame are illustrated in Fig. 8. The accelerograms exhibit a maximum magnitude of approximately one and two times the magnitude of the design ground acceleration of the frame, which was 0.30g. It must also be noted that the frequency of the acceleration motion was 3.277 Hz at the beginning and 2.521 Hz at the end (see Fig. 8).

The model was able to capture accurately the nonlinear response of the frame for all three sinusoidal accelerograms, reproducing the dynamic nonlinear ultimate limit state behaviour of the high ductility RC frame. For this reason, this model was used as the base of the numerical investigation performed on the SSI effect. The SSI models that were constructed for the needs of this research work, were analysed for the first and second sine-like acceleration motions as shown in Fig. 8.

It is important to note at this point that three types of soil are investigated and discussed in section 6, which assume hard (H), medium (M) and soft (S) stiffness according to Eurocode 8 standards [66] (types A, B and C, respectively). Table 2 depicts of the assumed material parameters of the soil types investigated, for two different soil depths of 6 m and 11 m.

Soil Type	Poisson ratio (v)	E (MPa)	G (MPa)	K (MPa)
Hard Soil (H)	0.3	5,000	1,923.08	4,166.67
Medium Soil (M)	0.3	700	269.23	583.33
Soft Soil (S)	0.3	65	25	54.17

Table 2. Soil Material properties used for the numerical investigation

The RC frame type H30 [50, 56] is analysed by assuming a soil domain of 21m x 10m and a depth equal to 6m for model A and 11m for model designated as B. Given that the total span of the RC frame is 3.2 m, by selecting a 21 m in length soil domain, it is anticipated that the dissipation of any waves that might be reflected at the boundaries of the soil mesh is minimized. This was also verified through visualizing the deformation shape of the soil mesh during the nonlinear dynamic analysis of the SSI numerical models. The SSI model with soil type A, is illustrated in Fig. 9. The dissipating ratio, for the investigation of the SSI effect on the dynamic behaviour of the RC frame was set equal to 5% for all the numerical models investigated in this research work.

It is also important to note at this point that the boundary nodes of the soil mesh were fixed, whereas no damping nor springs were used. This modeling approach was chosen based on the investigation performed on whether the boundaries of the under study nonlinear soil domain would develop reflective waves or dissipate the energy. According to the numerical investigation performed in this research work, it was found that the nonlinearities that were accounted through the Ramberg-Osgood material model in combination with the 5% dissipation ratio did not allow the development of reflective waves. Furthermore, an investigation on the method through which the accelerogram would be applied was also investigated. The accelerogram function was applied at the boundary nodes of the soil mesh, as shown in Fig. 9, while the option of applying the accelerogram at the nodes of the isolated footings of the RC frame was also explored. The results presented for this first RC frame were numerically obtained using the first approach. Finally, the foundation of the RC frame was assumed to be in full contact with the surrounding soil, in an attempt to avoid any additional modeling complications and numerical instabilities through the solution of a contact problem.

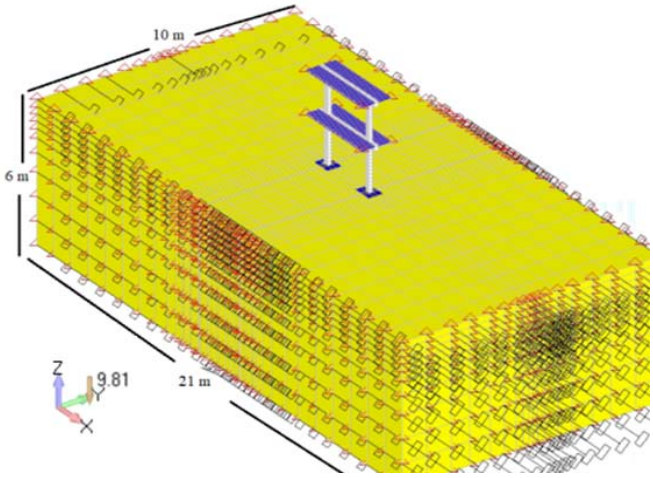

Figure 9. H30 frame model with soil model A.

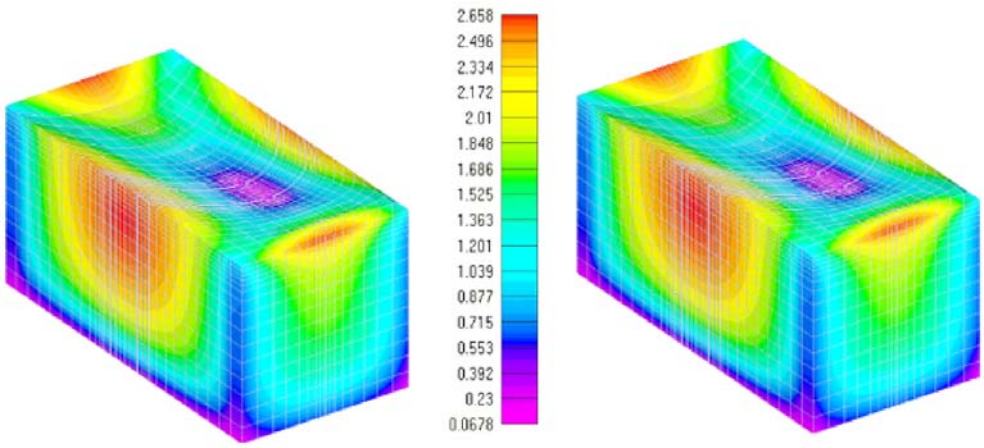

(a) (b)

Figure 10. Deformed shape and solid Von Mises contour at dynamic load increment 560. (a) Coarse and (b) fine soil mesh.

A mesh sensitivity analysis was performed prior to the main numerical investigation, using only the soil domain in order to verify that the developed soil mesh was not sensitive to mesh size effects. As it can be observed in Fig. 10, the analysis shows that the soil mesh with 1 m in size hexahedral elements along the z-direction (coarser mesh) gave the same results with the model discretized with a size of 50 cm (finer mesh). It must be noted here that the size of soil elements foresaw element sizes of 15-20 cm near the RC foundation, and the sizes are increasing when moving closer to the boundaries of the soil domain.

Based on the mesh sensitivity analysis performed, it was also found that there were no reflection waves developed at the soil mesh boundaries during the analysis of the numerical models, thus it was deemed sufficient to continue with those soil domain geometries and their assigned boundary conditions. The models that were analysed for different soil depths and soil properties are shown in Table 3.

	Soil depth	
Soil Type	6m (A)	11m (B)
Hard Soil	H30 R (A)	H30 R (B)
Medium Soil	H30 M (A)	H30 M (B)
Soft Soil	H30 S (A)	H30 S (B)

Table 3. Different models with different soil and geometrical properties.

The base-shear vs 2nd storey displacement curves with different soil parameters and depths are shown in Fig. 11. The curves present smooth hysteretic cycles, which is a phenomenon attributed to the capacity of the system to dissipate energy. It is evident [67], that the experimental fixed-base behaviour of the RC frame was appeared to have significantly less dissipated energy and the hysteretic loops presents excessive damage, which explains some pinching characteristics and the sequentially degradation of stiffness during the dynamic excitation. Table 4, presents the maximum displacement and maximum base shear forces for the examined models.

The differences observed between the SSI and the fixed-base models show that the largest divergence occurred in case of model H30 (S) B, where the base-shear is smaller than the fixed-based one by 21.2%. This is attributed to the SSI effect due to the soft soil assumption and the larger assumed soil depth that modifies the dynamic response of the frame during the nonlinear dynamic analysis. Furthermore, the maximum increase in the deformation was obtained for the case of model H30 (M) B, where the

maximum displacement is increased by 3.5%. This difference was found to be smaller than expected, a phenomenon attributed to the small size of the structure, which is translated into a relatively small mass that does not develop large inertia forces during this first set of dynamic loading. For this reason, the investigation proceeded with a larger in size RC frame, presented in the next section.

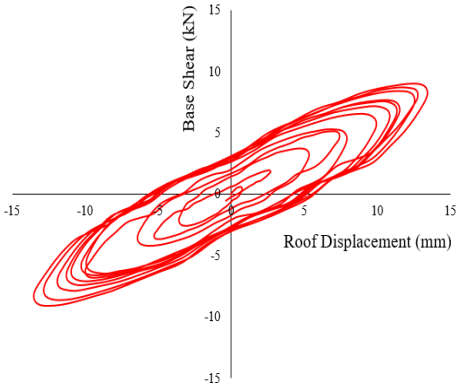

(a) Model H30 S (A)

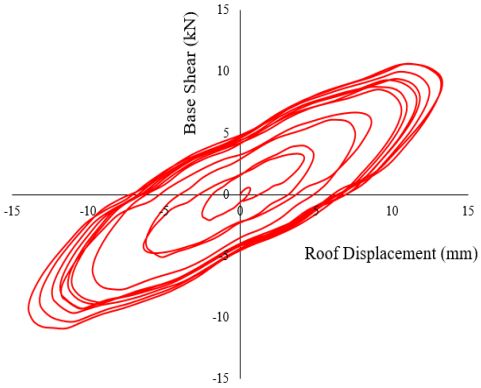

(b) Model H30 S (B)

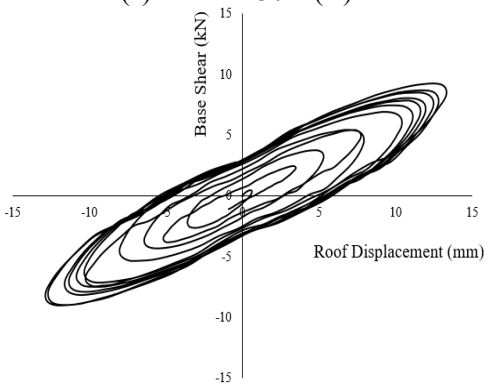

(c) Model H30 M (A)

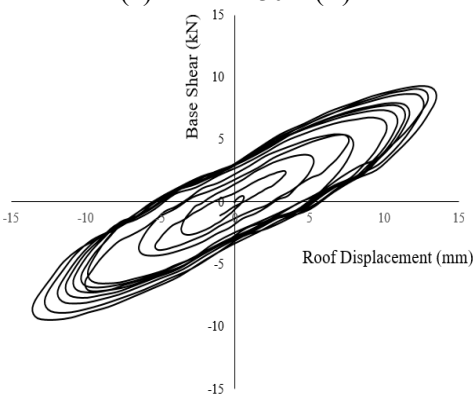

(d) Model H30 M (B)

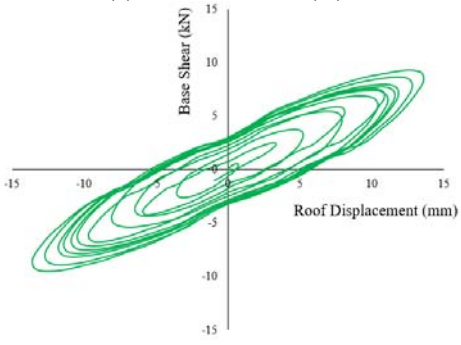

(e) Model H30 R(A)

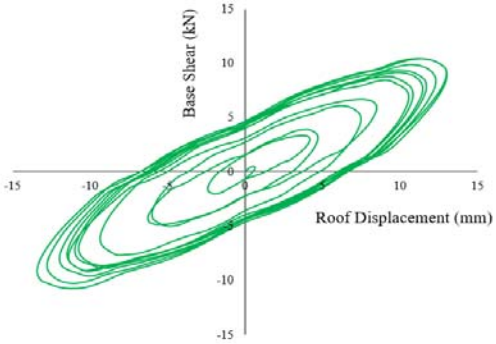

(f) Model H30 R (B)

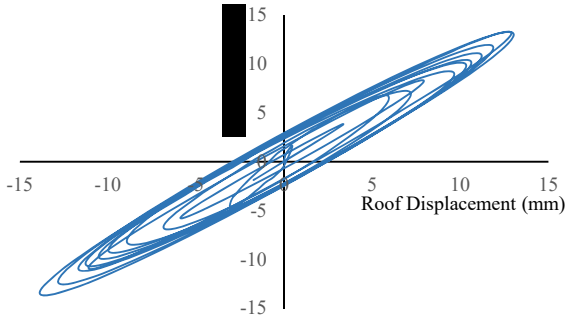

(g) Fixed Model H30 (F)

Figure 11. Base shear vs roof displacement for H30 models

	Max Displacement δ (mm)	$\frac{(\delta_{SSI}-\delta_{fixed})}{\delta_{fixed}}$ (%)	Max Base Shear V (kN)	$\frac{(V_{SSI}-V_{fixed})}{V_{fixed}}$ (%)
H30 R(A)	13.7	4.8	9.5	-30.9
H30 M(A)	13.3	2.2	9.3	-32.3
H30 S(A)	13.6	4.0	9.1	-33.4
H30 R(B)	13.4	3.0	10.8	-21.5
H30 M(B)	13.6	4.1	9.4	-31.2
H30 S(B)	13.9	6.8	10.9	-20.3
H30 F	13.0	-	13.7	-

Table 4. Maximum roof displacement and base shears of the H30 frame models.

Before discussing the findings from the study of a larger RC frame, Table 5 is given herein where the maximum dissipated-energy that was developed during the nonlinear dynamic analysis is presented for each model. It is easy to observe that the SSI model with the larger soil domains (11 m soil depth) derived increased dissipated energies compared to the corresponding models with smaller soil domain (6 m soil depth). It is also noticeable that the hard soil models present a larger amount of dissipated energy than the soft and medium soil domains. This is a numerical phenomenon attributed to the severe damages that the RC frame developed combined with the dissipation mechanism from the soil domain during the nonlinear analysis for the case of the H30 R(A) and H30 R(B) models.

	Max dissipated energy (kN·mm)	Increase compared to the fixed-base model (%)
H30 R(A)	159.13	29.08
H30 M(A)	144.93	17.56
H30 S(A)	153.27	24.33
H30 R(B)	212.47	72.35
H30 M(B)	158.47	28.54
H30 S(B)	221.27	79.49
H30 (F)	123.28	-

Table 5. Maximum dissipated energy of the H30 frame models.

On the other hand, the fixed model that suffered the most amount of damage during the analysis, did not appear to derive large dissipated energy because of its low dissipating mechanisms (hysteretic material behavior of the superstructure and viscous damping). This also highlights the contribution of the soil domain in-terms of

dissipating the seismic energy during the nonlinear dynamic analysis. Finally, the soft soil models present the largest dissipating energies due to the additional flexibility added to the system at the foundation level that causes the frame to develop larger hysteretic loops.

4.2. RC Frame Building with 4 Columns

The RC frame building that is examined in this section, consists of the two previous plane frames H30, connected with slabs, as illustrated in Fig. 13 and notated as 2H30. The model has been analysed with the same seismic excitation as the previous model in Fig. 8 (first sine-like acceleration). A model with fixed-base conditions shown in (Fig. 12a) denoted as 2H30(F) is also studied. The excitation is applied at the base of the foundation domain for the SSI models and for the fixed-base conditions, the seismic motion is also applied through the foundation nodes of the frame. Furthermore, the fixed-base model and the SSI models with 6m depth are analysed for the first sine-like acceleration of Fig. 8. The SSI models were analysed for the medium and soft soil cases, given that the hard soil model was found to derive similar results to the fixed-base model. The damping ratio that is used for the dynamic nonlinear analysis was set to 5%.

Table 6 depicts the maximum displacement and base shear forces that are developed in the 2H30 frame building model with different soil properties and depths. Based on the obtained numerical results, the fixed-base model gave a maximum of 6.5 mm horizontal deformation at the top slab, while the maximum base shear was found equal to 73.5 kN. As it is shown in Table 6, the SSI model with 6m in depth soft soil produced the highest horizontal displacement increase (92% increase), while the 11 m depth medium soil SSI model derived the smallest increase in terms of horizontal displacement (13.7%). According to the obtained numerical results, the model with the deeper soil domain gave a smaller displacement increase when compared with the respective models with the same soil depths.

The results show that the SSI models induced greater flexibility and the computed displacements are higher than the 2H30(F) model for all analysed models. For the case of the maximum developed base-shear, it is noted that the same phenomenon is observed with the maximum base-shear increase to be equal to 32.5% for the case of the 2H30 S(A) model.

a)

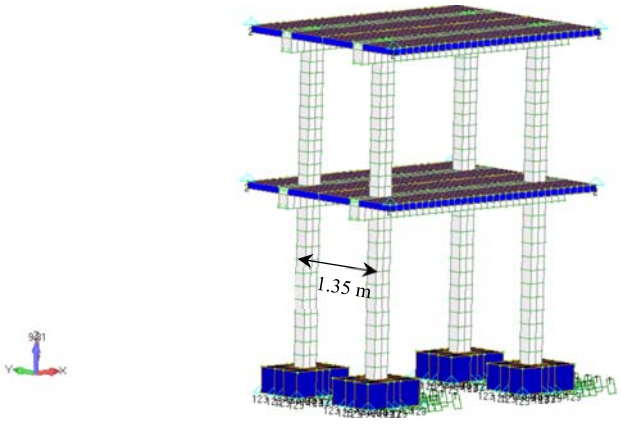

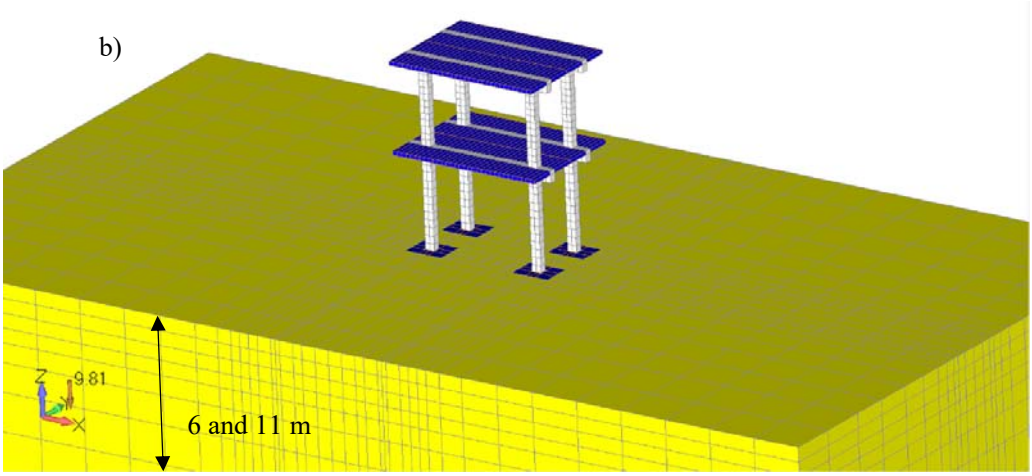

Figure 12. Four-column frame building 2H30 with soil depth a) fixed-base and b) 6m (A) and 11m (B).

	Max Displacement δ (mm)	$\frac{(\delta_{SSI}-\delta_{fixed})}{\delta_{fixed}}$ (%)	Max Base Shear V (kN)	$\frac{(V_{SSI}-V_{fixed})}{\delta V_{fixed}}$ (%)
2H30 M(A)	8.03	23.4%	80.08	9.0%
2H30 S(A)	12.5	92.1%	97.30	32.5%
2H30 M(B)	7.40	13.7%	73.60	0.2%
2H30 S(B)	11.71	79.9%	92.17	25.5%
2H30 (F)	6.51	-	73.45	-

Table 6. Maximum Displacement and Base shears of the L30 frame models.

Figs. 13 and 14 show the horizontal displacement curves vs time as well as in Figs. 15 and 16 the total base shear curves vs time as they derived from the nonlinear dynamic analysis of the fixed-base and SSI models. It is evident that the softer the soil is, the larger the computed horizontal displacement and the developed base shear. It is also observed that after the 3 first loading cycles are applied (1 second after the seismic excitation begins), the horizontal displacements of the SSI models become larger than those derived from the fixed-base model. This phenomenon was initially attributed to the method through which the accelerogram was applied that did not foresee the solution of an initial load step by applying only the static loads and then apply the accelerogram through the nonlinear dynamic algorithm. Given that the analysis assumes that the full self-weight of the RC frame is applied at the first dynamic increment, a dynamic phenomenon is developed at the first half a minute, which foresees the vertical oscillation of the frame.

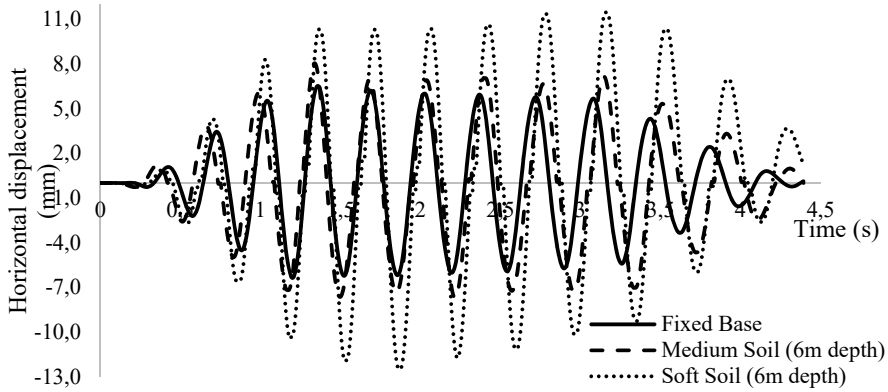

Figure 13. RC frame building. Horizontal displacement vs time curve. Fixed-base model vs models with 6 m in depth soil (A).

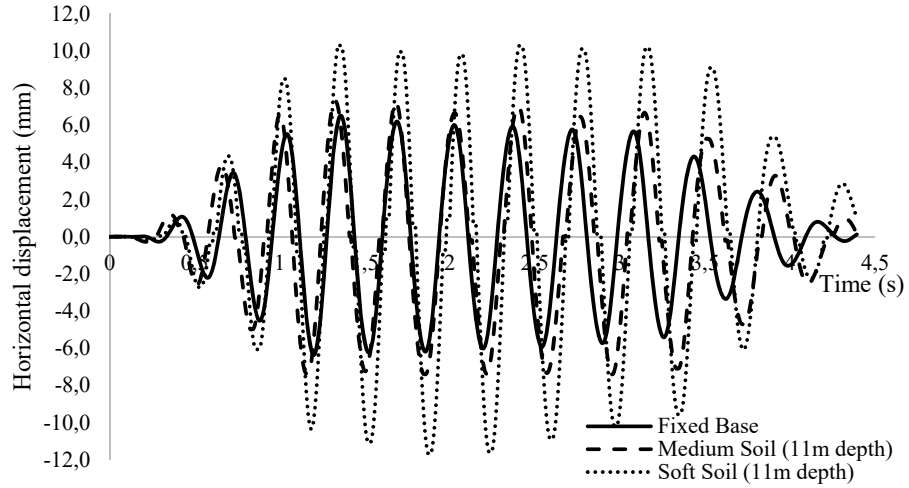

Figure 14. RC frame building. Horizontal displacement vs time curve. Fixed-base model vs models with 11 m in depth soil (B).

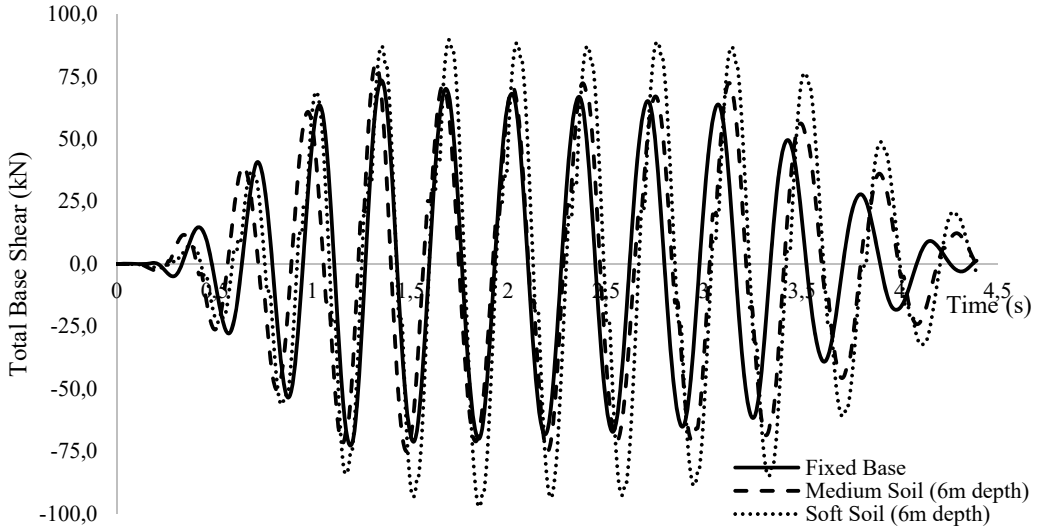

Figure 15. RC frame building. Total base shear vs time curve. Fixed-base model vs models with 6 m in depth soil (A).

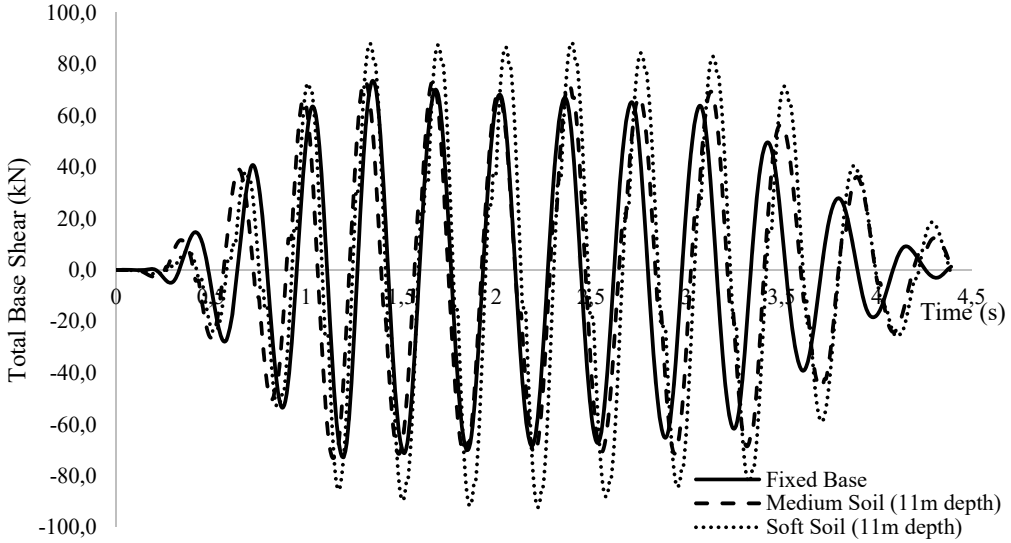

Figure 16. RC frame building. Total base shear vs time curve. Fixed-base model vs models with 11 m in depth soil (B).

This phenomenon is illustrated through the base reactions curve vs time in Fig. 17, where the reactions along the global x and z directions are plotted. The global x direction represents the horizontal in-plane direction of the plane, where the global z direction is parallel to the gravitational loads. As it can be seen in Fig. 17, the soft soil model develops a vertical oscillation that generates a respective vertical reaction due to the dynamic movement along the gravitational axis. Nevertheless, it is evident that the developed vertical base reaction tends to stabilize after 0.4 seconds pass by, thus as it is going to be illustrated at a later stage in this section, this was not the reason of the increase of the base shear.

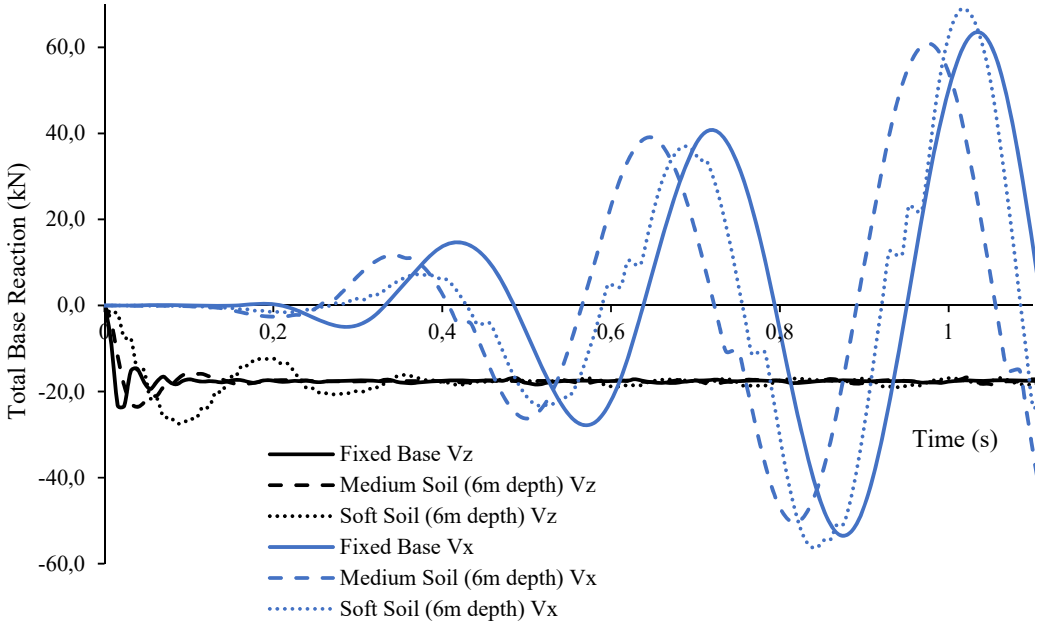

Figure 17. RC frame building. Total base reactions vs time curve. Fixed-base model vs models with 6 m in depth soil (A).

4.2.1 Fundamental frequency evaluation

In order to further investigate the obtained SSI dynamic response of the RC frames, the fundamental frequencies of the stratum were computed (see Table 7) according to the typical frequency equations:

$$f_S = \frac{V_s}{4H} \tag{29}$$

$$f_{SV} = \frac{3.4}{\pi(1-\nu)} f_s \tag{30}$$

where V_S is the velocity of shear waves within the soil, f_S the fundamental frequency along the horizontal axis, f_{SV} the fundamental frequency along the vertical axis ("compression" mode) and H is the soil depth. The fundamental periods of the examined soil domains were numerically computed through the typical Eqs. (29-30) and through the modal analysis of the FEM models, and are presented in Table 6. It can be observed that the discrepancies between the calculated frequencies derived from modal analysis and the Eqs. 29-30 are significantly large. This indicates the fact that the use of Eqs. 29-30 provides a rough estimation of the fundamental frequencies of the soil domain. Additionally, the modal analysis takes into account the boundary

conditions, the stiffness and the mass of the soil domain but it does not use the velocity of shear waves within the soil. Table 8 shows the first 3 numerically computed frequencies of the RC frame according to its boundary conditions (with and without SSI). A comparison is also provided in Table 8 between the computed frequencies of the 2H30(F) model and those derived from the SSI model. It is obvious that the fixed model exhibits the stiffest behaviour out of the 6 SSI models (including the models with soil type A, rock).

It can be observed that the model with medium soil depth equal to 6 m gives a fundamental frequency f_S equal to 5.1 Hz computed by the Eqs. 29-30, which is closer to the 1st fundamental frequencies of the SSI models (6.0-7.1 Hz as shown in Table 8). Additionally, close to the above frequency range of the SSI models is the fundamental frequency computed by the modal analysis of the model with soft soil depth equal to 11 m. Furthermore, the 2nd frequency of the SSI models is close to the f_{SV} derived from the modal analysis of the medium soil models. Fig. 18 shows the modal shapes of the fixed-base model and the SSI models of the series (B) for the case of 11 m depth of the soil domains. It is easy to observe that Fig. 18h shows a vertical oscillation of the RC frame founded on a soft soil domain.

		Soft Soil		**Medium Soil**	
		Depth (m)			
		6	**11**	**6**	**11**
Typical Frequency Eq. (29-30)	**f_S (Hz)**	1.553	0.847	5.096	2.780
	f_{SV} (Hz)	2.401	1.310	7.879	4.297
	$T_{(x)}$ (sec)	0.644	1.181	0.196	0.360
	$T_{(z)}$ (sec)	0.417	0.764	0.127	0.233
Modal Analysis FEM	**f_S (Hz)**	8.39	7.25	27.52	20.46
	f_{SV} (Hz)	9.24	4.96	30.36	16.27
	$T_{(x)}$ (sec)	0.12	0.14	0.036	0.049
	$T_{(z)}$ (sec)	0.11	0.2	0.033	0.061

Table 7. Fundamental frequencies and periods of the soil domains.

Model	1st Eig.freq.	$\frac{(f_{SSI}-f_{fixed})}{f_{fixed}}$ (%)	2nd Eig.freq.	$\frac{(f_{SSI}-f_{fixed})}{f_{fixed}}$ (%)	3rd Eig.freq.	$\frac{(f_{SSI}-f_{fixed})}{f_{fixed}}$ (%)
2H30 R(A)	7.04	-0.34	19.78	-0.14	30.51	-0.45
2H30 M(A)	6.91	-2.14	19.63	-0.86	29.60	-3.40
2H30 S(A)	5.95	-15.74	17.90	-9.63	18.41	-39.91
2H30 R(B)	7.04	-0.34	19.78	-0.14	30.50	-0.48
2H30 M(B)	6.91	-2.18	19.63	-0.87	29.49	-3.76
2H30 S(B)	5.94	-15.97	17.12	-13.54	18.41	-39.93
2H30 (F)	7.06	-	19.81	-	30.64	-

Table 8. Comparison of the first three eigenfrequencies for four-column frame building 2H30 models.

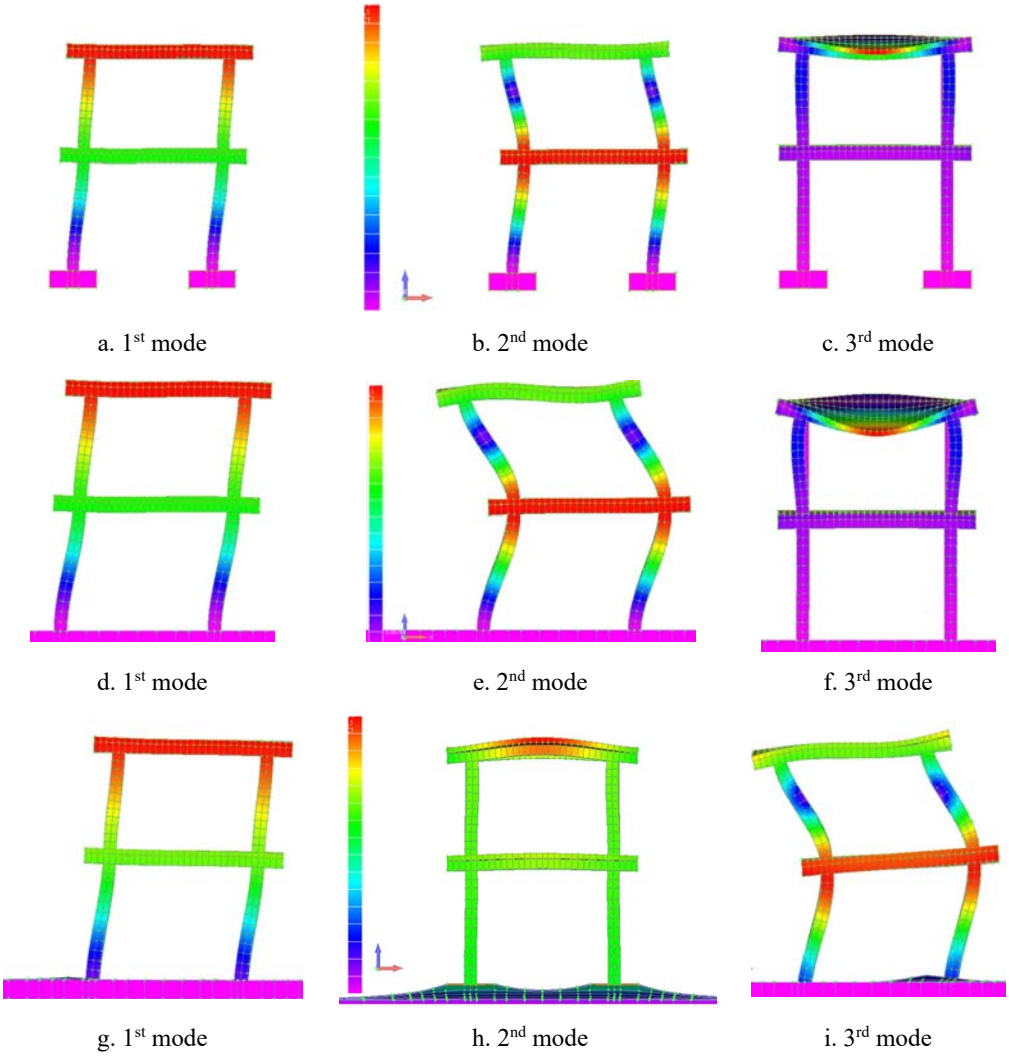

a. 1st mode b. 2nd mode c. 3rd mode

d. 1st mode e. 2nd mode f. 3rd mode

g. 1st mode h. 2nd mode i. 3rd mode

Figure 18. Deformed shapes for the first 3 modes for four-column frame building (a-c) Fixed, (d-f) Medium and (g-i) Soft soil. Case of soil depth 11m.

4.2.2 Hysteretic curves and soil vertical deformations

Before moving to the last stage of this investigation with the nonlinear dynamic response of the 2H30(A) models under larger dynamic loading conditions, the hysteretic curves of the 5 under study models are shown in Fig. 19. It is evident that the SSI models exhibit a larger energy hysteresis attributed to the soil nonlinearities developed during the dynamic analysis. The soft soil exhibited SSI models the highest energy dissipation, highlighting the significant effect of the SSI phenomenon. The maximum developed dissipated energy for each model is presented in the Table 9. It is evident that the 2H30 (F) model developed the smallest dissipated energy during the dynamic analysis. The dissipated energy was produced by the 2H30 S(A) model which is larger than the one derived from the fixed model by 360.78%. It must be noted here that, the hysteretic curves presented in this work refer to the total base shear computed at the base of the structure vs the horizontal displacement at the roof of the RC frames excluding the rigid body horizontal displacements.

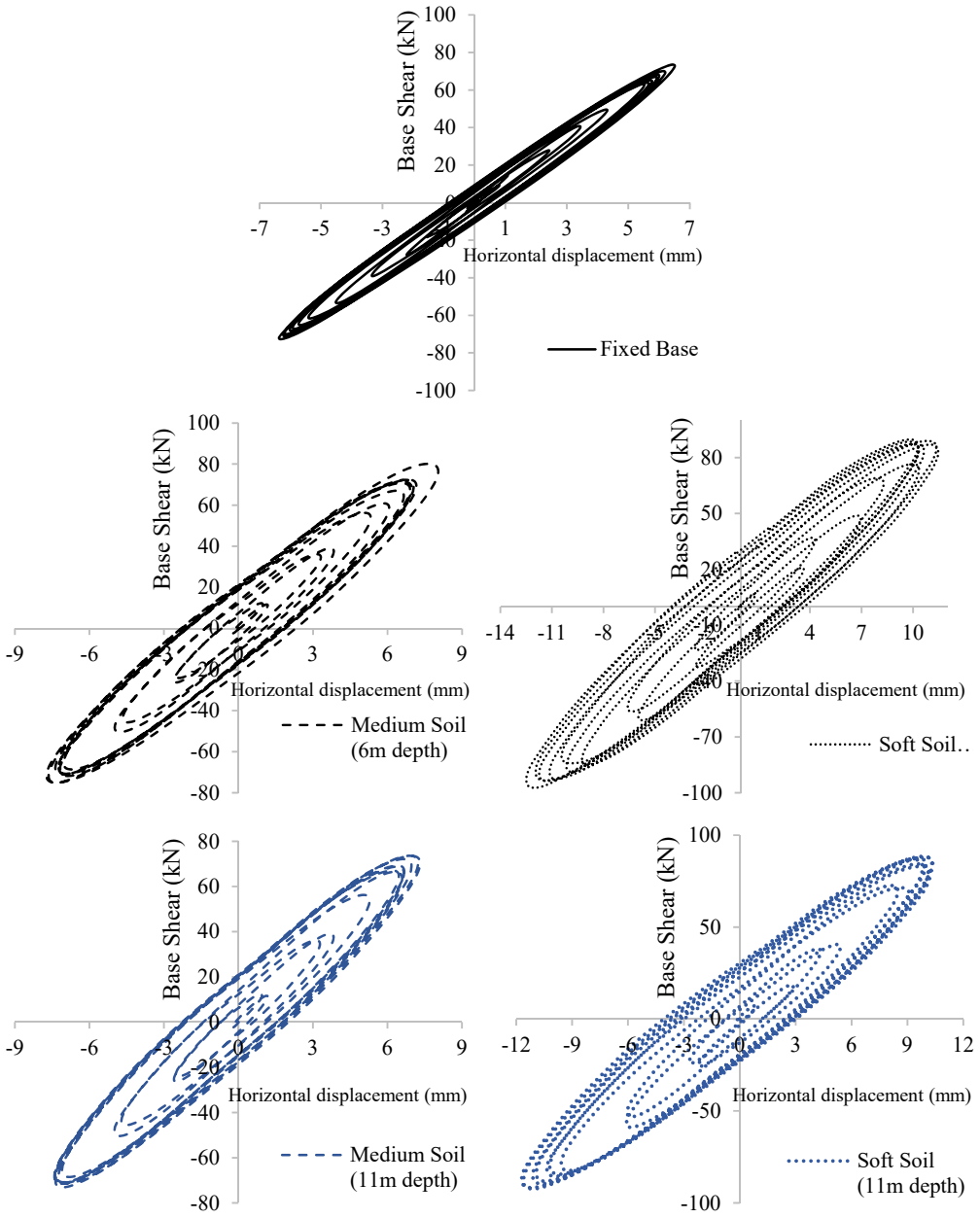

Figure 19. RC frame building. Hysteretic curves.

	Max dissipated energy (kN·mm)	Divergence from fixed model (%)
2H30 M(A)	547.94	171.63
2H30 S(A)	929.49	360.78
2H30 M(B)	426.57	111.47
2H30 S(B)	908.1	350.18
2H30 (F)	201.72	-

Table 9. Maximum dissipated energy of the 2H30 frame models.

Furthermore, the vertical deformation of the boundary node is plotted in Fig. 20 for both 2H30 M(A) and 2H30 S(A) models, to investigate the level of vertical oscillation of the waves that reach the boundaries of the soil domain. It can be seen that the largest

vertical deformation -0.54 mm occurs for the soft soil case, where the corresponding deformation for the medium soil domains was computed to be equal to -0.33 mm. This indicates that the intensity of the waves that reach the west and east boundaries of the soil domains are very small and do not affect the dynamic response of the RC frame. Thus, the assumed boundary conditions of fixing the x and y boundary degrees of freedom and allowing the vertical deformation of the soil nodes was found an acceptable modelling approach.

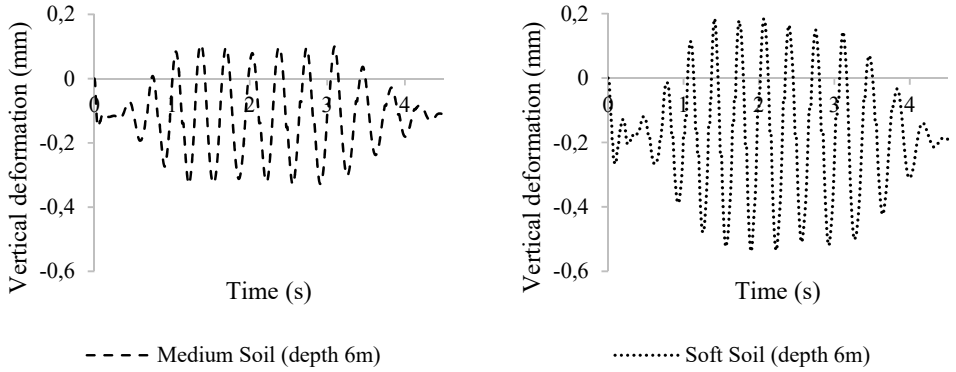

Figure 20. RC frame building. Vertical deformation vs time curves of the boundary soil node with the largest deformation.

4.2.3 Analysis for the first two consecutive accelograms

To further investigate the SSI effect under nonlinear dynamic ultimate limit state loading conditions, the fixed-base and the SSI models with 6 m in depth of soil domain were analysed for the first two accelerograms shown in Fig. 8. The frequency of the 2nd acceleration motion was 2.395 Hz at the beginning and 1.846 Hz at the end. The derived displacement curves vs time are given in Fig. 21, where the nonlinear dynamic response of the fixed-base model is compared to those obtained from the two SSI models.

According to Fig. 22, the fixed-base model manages to resist to the developed inertia forces during the two consecutive accelerograms developing a 2.5 mm remaining horizontal displacement at the 2nd storey. The maximum horizontal displacement developed by the fixed-base model was 15.04 mm (see Table 10), where the maximum base shear obtained from the nonlinear dynamic analysis was 114.4 kN.

On the other hand, the 2H30 M(A) model was found to develop an unstable behaviour after the 9th second of the applied accelerogram, exhibiting severe damages at the ground floor columns of the RC frame. This instability that eventually led to an excessive maximum horizontal displacement of 37.85 mm and a remaining deformation of 24 mm (at the end of the dynamic excitation), attributed to the SSI effect and the dynamic behaviour of the RC frame building and the soil domain that interact during the nonlinear analysis. It is also reasonable to say at this point that the vertical oscillation and the respective reaction shown in Fig. 17 do not affect significantly the base shear developed within the SSI models during the first accelerogram. As it can be seen in Figs. 21 and 22, the 2H30 M(A) and fixed-base models are found to have no horizontal deformations when the second accelerogram is imposed at the two models, where the SSI model develops larger horizontal displacements and base shear during this larger dynamic excitation. According to Table 10, the 2H30 M(A) model developed almost 5 times larger horizontal deformations compared to the fixed-base model, where its maximum base shear was found to be 7.3% larger as well.

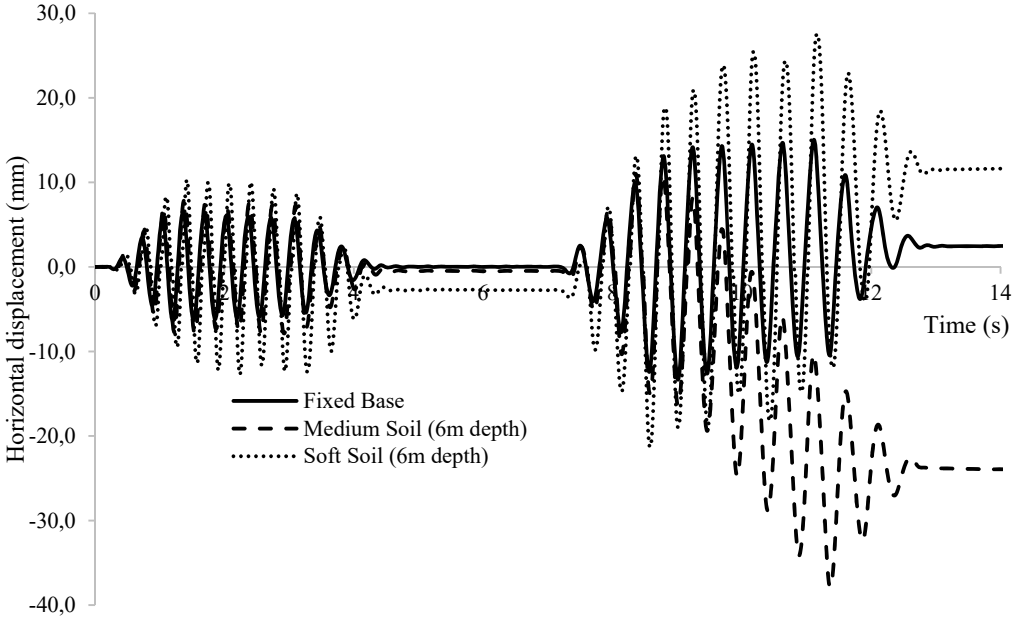

Figure 21. RC frame building. Horizontal displacement at the 2nd storey vs time curve. Two accelerograms.

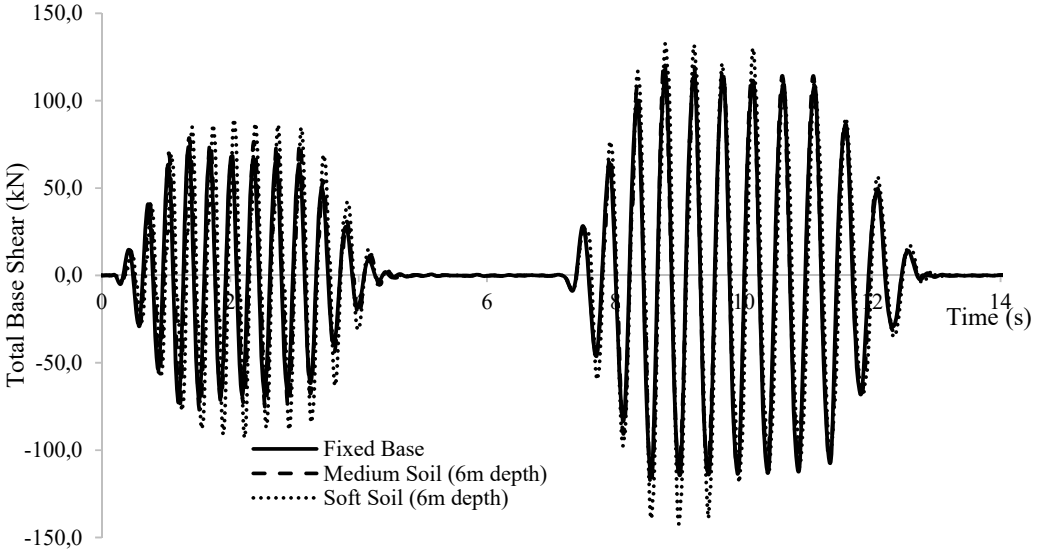

Figure 22. RC frame building. Total base shear vs time curve. Two accelerograms.

An additional finding that can be extracted from the derived numerical results, is that the softer the soil is, the larger the base shear increase is for the case of the under-study structure (see Table 10). Furthermore, the complexity of the SSI effect when nonlinearities are accounted for at both superstructure and soil domains, is highlighted by the fact that the RC frame was found to develop a remaining horizontal deformation of 2.7 mm after the completion of the first dynamic excitation. One would have expected this RC frame to develop additional damages and eventually become unstable earlier than the building of model 2H30 M(A), that assumes a medium soil domain and had close to zero permanent deformation after the 1st acceleration. Both SSI models with soft and medium soil reached failure during the 2nd accelerogram. However, the SSI model with the medium soil became unstable quicker than the soft soil model and developed a significantly larger remaining horizontal deformation at the end of the

dynamic analysis.

In order to further investigate and justify the obtained nonlinear dynamic responses, the natural frequencies were numerically computed and recorded at every dynamic load increment through performing a modal analysis of the RC structure. Fig. 23 shows the fundamental frequencies as they resulted from the nonlinear dynamic analysis of the 2H30 (F), M(A) and S(A) models. It is easy to observe that the fixed-base model derives the highest frequency at the beginning of the analysis, but due to the development of cracks from an early stage of the analysis it becomes more flexible compared to the SSI models. This mechanical response is caused by the damage development at the columns of the RC structure due to the fixed support conditions that lead to an early strain development at the columns of the ground floor.

It is also important to observe that the decrease of the 1st natural frequency of the soft soil model 2H30 S(A) is smaller than both the fixed-base and the medium soil models. This attribute shows that the flexibility of the system of the soft soil model causes the RC frame to develop lower levels of damage compared to the fixed-base and medium soil models. This finding also partially explains why the fixed-base model developed the largest level of damage especially at the beginning of the analysis, resulting the smallest base shear out of the three models.

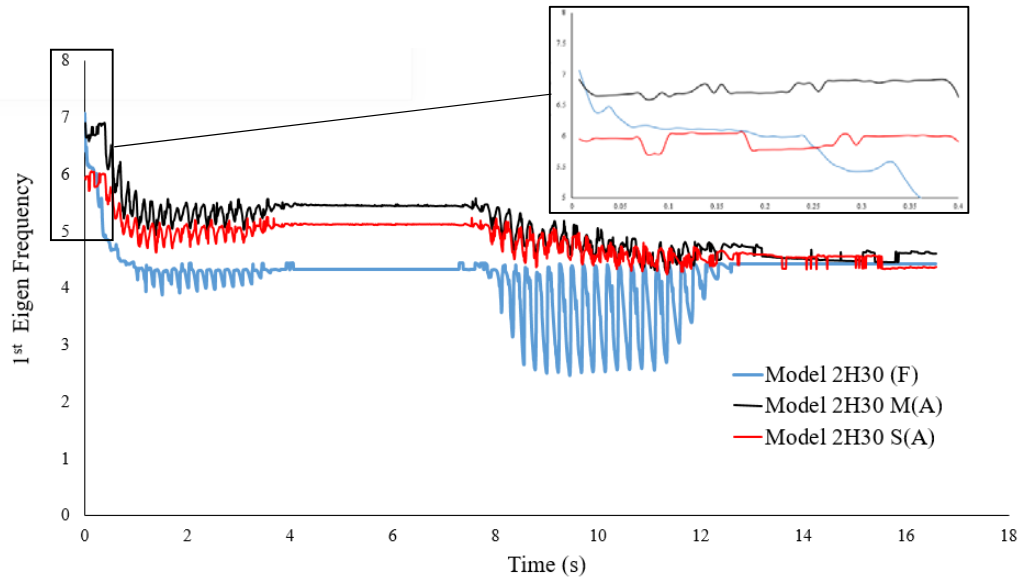

Figure 23. 1st Eigen frequency calculated through time for 2H30 models

During the 2nd accelerogram (7-14 seconds of the analysis), both models 2H30 M(A) and S(A) become unstable due to failure near the top of the columns at the lower level of the building. Based on the frequencies graph the medium soil model reached the state of resonance first given that the structure's 1st natural frequency was equal to 5 Hz at around 9 s, which was found to be close to the soil's frequency calculated by Eqs. 29-30 as shown in Table 7. This is also evidence that the devolvement of large deformations that derived from the SSI models after the 9th second of the nonlinear dynamic analysis is attributed to the change recorded in-terms of flexibility of the RC structure compared to the flexibility of the soil domain and the relevant interaction of the soil domain and the damaged RC frames. This was not the case for the fixed-base model that was assumed to be rigidly fixed at its base, where it maintained its stability throughout the analysis.

To further investigate the differences between the medium and soft soil models, the

deformed shape of the two models are depicted in Fig. 24 for different dynamic load increments. Fig. 24a shows the deformed shape at dynamic increment step 1,115 (8.64 second), which represents the step at which the 2H30 M(A) model starts to develop damages at the columns of the ground floor, which triggered the unstable dynamic response that led to the significant damages predicted from the analysis. Figs. 24b and 24c show the magnified deformed shapes of the RC frame at dynamic load steps 1,156 and 1,285, respectively, where it can be seen that the columns of the RC frame develop permanent deformations due to the concentrated strains that are developed at the lower level of the building.

The areas that appears to fail due to shear deformation, are located close to the areas where the critical length at the top of the columns ends. This indicates that the cracking that was developed within the structure surpassed the critical area for the case of the SSI models due to the shift of the damage regions. At the height where the amount of stirrups is lower than the one of the critical area, the columns have decreased ductility and strength, thus fail in shear. This shows that the most vulnerable areas for the examined SSI models, are the ones where significant change of shear stiffness takes place, leading to column failure. Additionally, the ability of the footings to rotate due to the soil domain re-distributes thus shifts the crucial regions that can lead to a different failure mechanism compared to the fixed-base model.

To further highlight the differences between the two models, the magnified deformations of the soil around the footings of the two SSI models are given in Fig. 25. The deformations at the dynamic load increment 1,285 are shown with a magnification scale factor of 4,000 and 1,000 for the case of 2H30 M(A) and 2H30 S(A) models, respectively. It is evident that the soft soil model develops significantly larger deformations (approximately 10 times larger) allowing the footing to rotate during the dynamic excitation. Nevertheless, the computed maximum settlement due to the superstructure loads at this dynamic time step was found to be around 0.08 mm for the soft soil model and a 0.008 mm for the medium soil model, which was found to be small. Furthermore, the softer soil behaviour at the foundation level, led the 2H30 S(A) model in developing smaller horizontal deformations at the 2nd storey level near the failure of the RC structure.

	Max Displacement δ (mm)	$\frac{(\delta_{SSI}-\delta_{fixed})}{\delta_{fixed}}$ (%)	Max Base Shear V (kN)	$\frac{(V_{SSI}-V_{fixed})}{\delta V_{fixed}}$ (%)
2H30 M(A)	37.85	481.5%	122.74	7.3%
2H30 S(A)	27.53	323.0%	142.17	24.3%
2H30 (F)	15.04	-	114.40	-

Table 10. Maximum Displacement and Base shears of the H30 frame models.

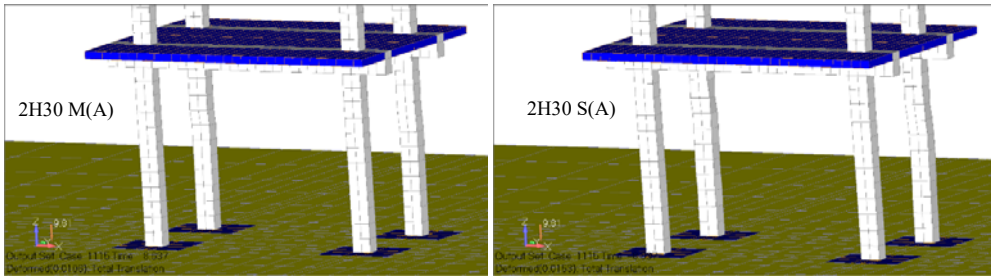

a. Dynamic time step 1,115

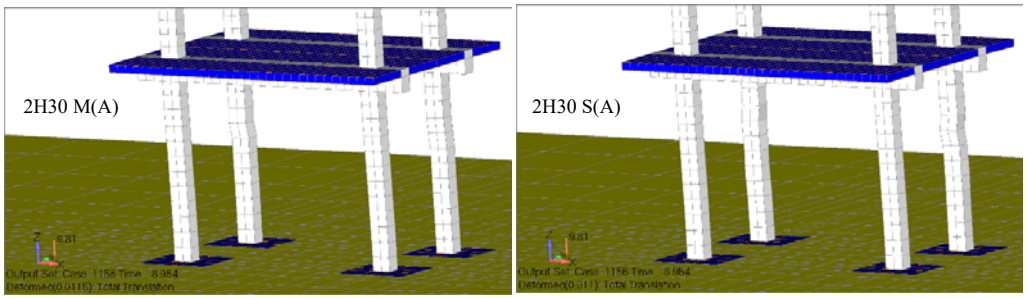

b. Dynamic time step 1,156

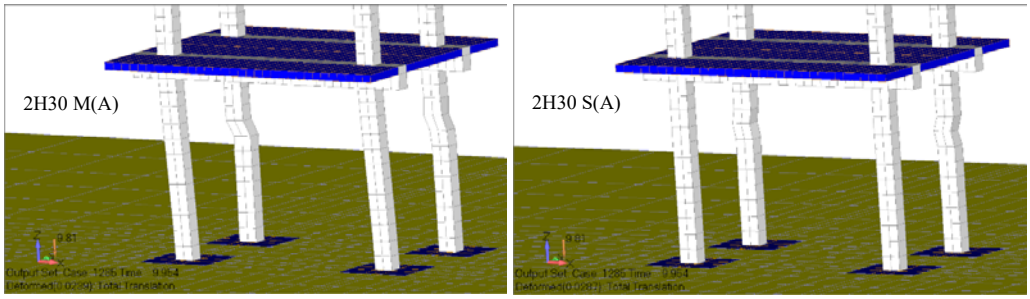

c. Dynamic time step 1,285

Figure 24. RC frame building. Deformed shapes of the superstructure at different time steps. Magnification scale factor 5x.

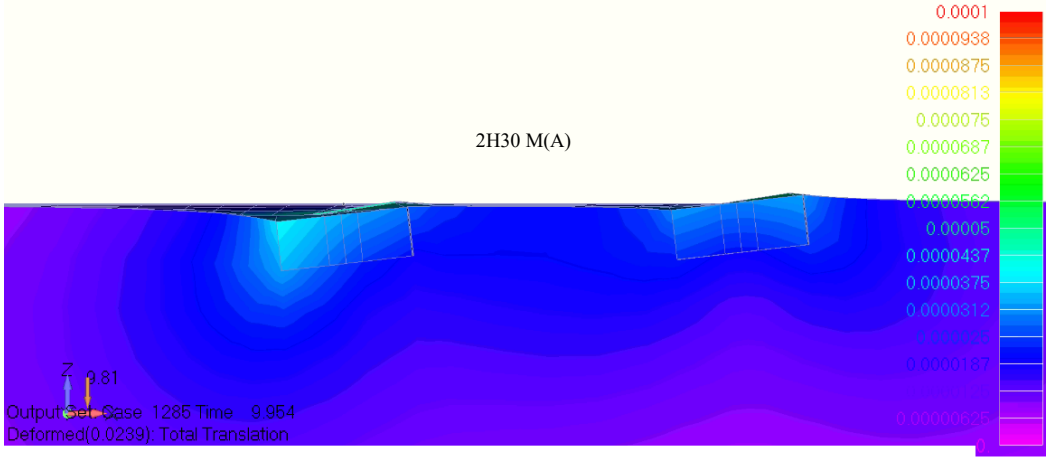

Magnification scale factor 4,000x

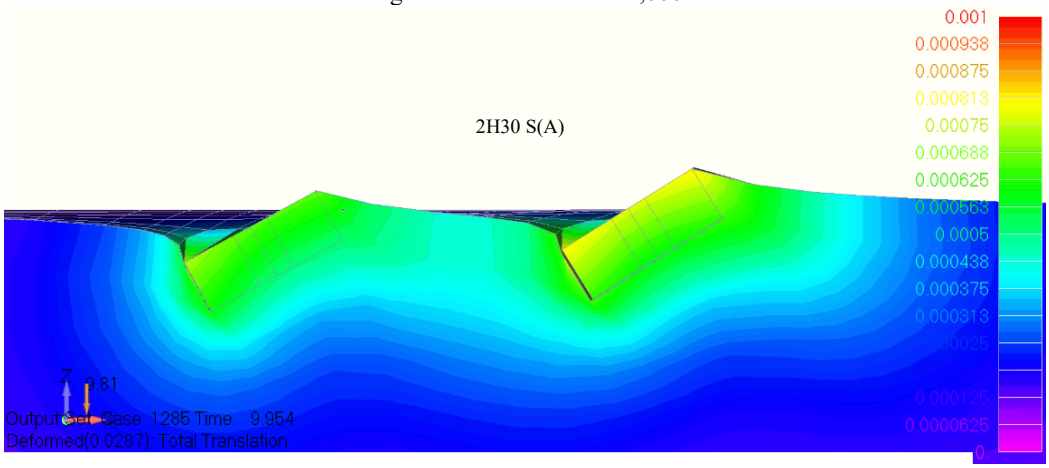

Magnification scale factor 1,000x

Figure 25. RC frame building. Deformed shapes of the soil domain at dynamic load step 1,285.

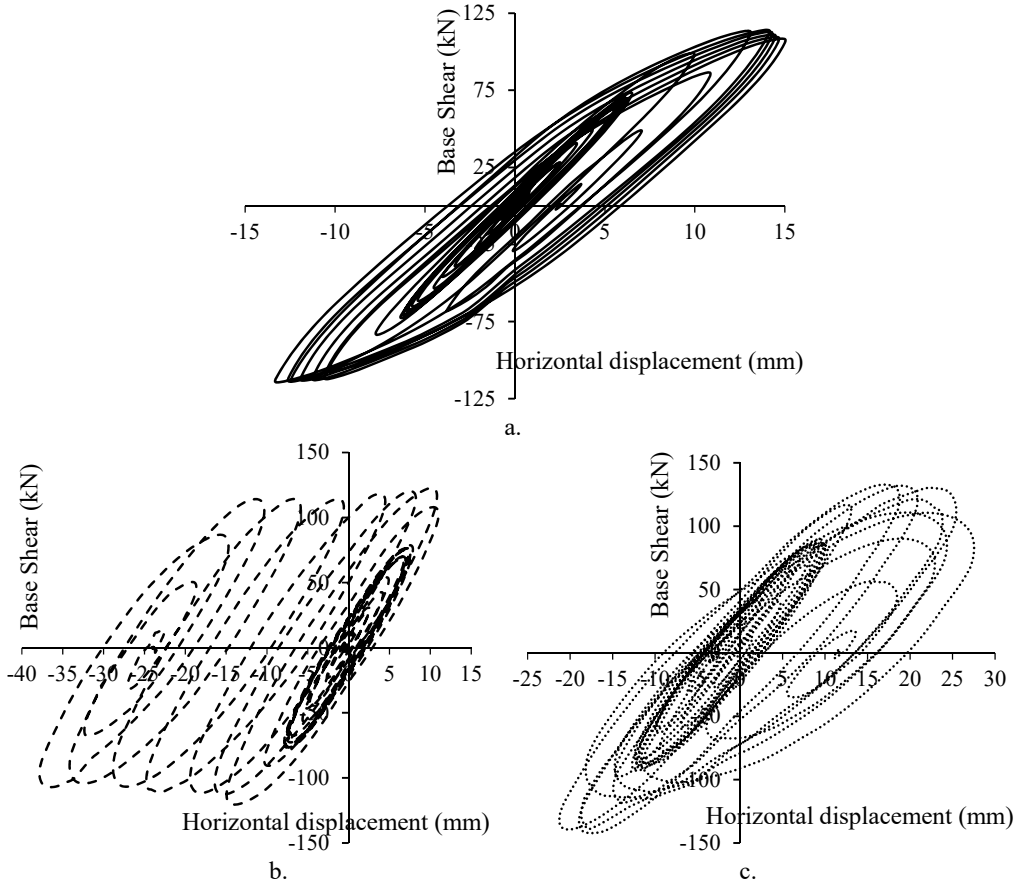

Figure 26. RC frame building. Hysteretic curves derived from the analysis of the two accelerograms. a) Fixed-base (2H20(F)), b) medium (2H30 M(A)) and c) soft (2H30 S(A)) soil models.

Fig. 26 shows the hysteretic curves as they resulted from the nonlinear dynamic analysis of the three models that were investigated for the case of the two accelerograms. It is easy to observe that the medium soil domain model 2H30 M(A) exhibits the largest horizontal deformation, but it is the soft soil domain model 2H30 S(A) that achieves the largest energy dissipation (32,880.4 kN mm) out of the three models. The fixed-base model derived a total of 10,796.6 kN mm energy dissipation and the 2H30 M(A) model derived a respective 17,589 kN mm. This is attributed to the nonlinearities developed at the soil domain around the isolated footings, especially during the 2nd imposed accelerogram.

4.2.4 Nonlinear Pushover Analysis of the SSI models

A pushover analysis was also conducted to test the impact of the soil on the 4-column RC frame. According to [56], the maximum spectral accelerations that derives for the first earthquake simulation test is $S_a = 2.153g$, which was significantly larger than the design spectral acceleration (Eurocode 8, Soil type B, $S_a = 0.75g$). The lateral load was applied assuming a triangular distribution that mainly represents the first vibration mode. The P-δ curves are presented in Fig. 27 as they resulted from models 2H30 (F), S(A), M(A), S(B) and M(B). The roof displacement is measured relatively to the foundation displacement for each model, where the initial linear behavior of the soft soil model was found to derive more flexibility than the medium soil and the fixed-base models.

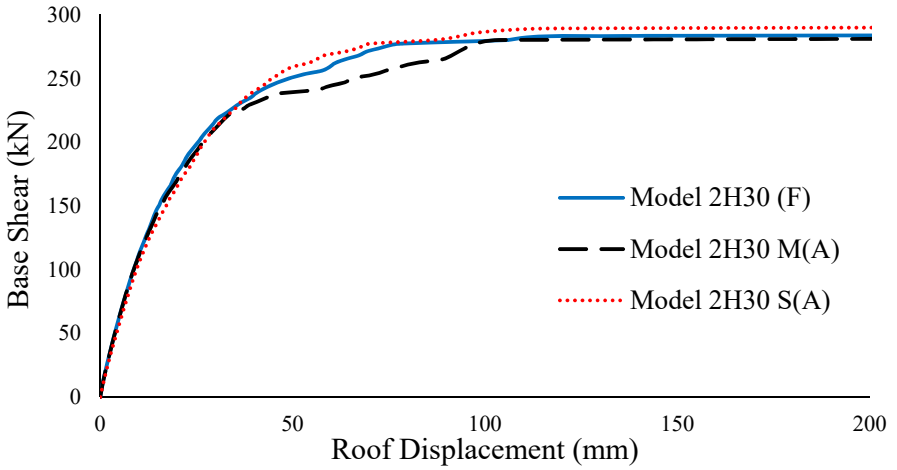

(a)

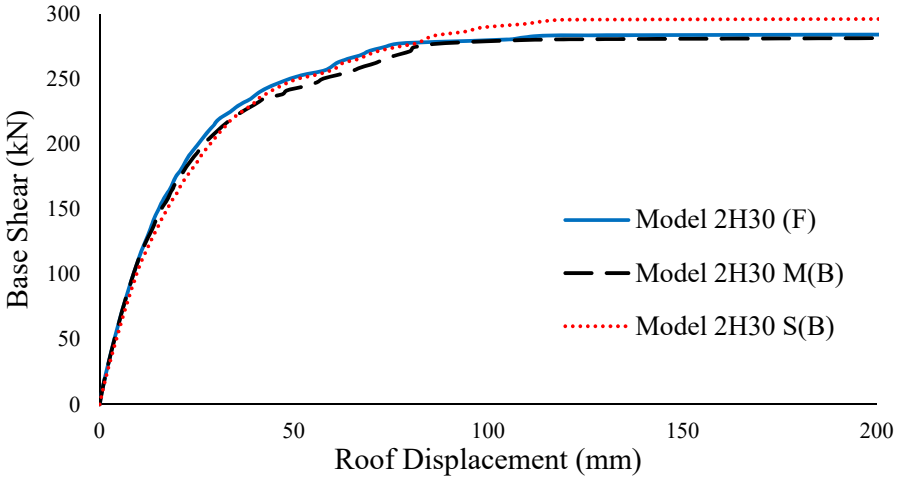

(b)

Figure 27. 4-column RC frame building. Pushover analysis considering soil with depth equal to a) 6 m and b) 11 m.

According to the overall mechanical response, it was found that the medium soil model suffers from major damages earlier than the other models. In order to explain this phenomenon, Fig. 28 shows the von Mises strains that are developed in the RC frames for a roof displacement close to 30 mm. At this stage, the medium soil models 2H30 M(A & B) develop a significant decrease of their stiffness for the first time. Once more this is attributed to the damage re-distribution that causes different areas of the frame to develop concentrated strains during the pushover analysis.

The soft soil models 2H30 S(A &B) present a larger rotation at the foundation level and the maximum strain concentrations were found to occur at the lower columns and mainly at the West column near the base. On the other hand, the medium soil models developed the largest strains at this stage, which were concentrated at the right column of the lower storey. The concentration of larger damage outside the critical column regions at the ground floor, made the medium soil models more flexible than the other models after the roof horizontal displacement exceeded 30 mm.

As the pushover analysis continued, the fixed-base model was found to develop concentrated damages at the columns found at the ground floor, suddenly decreasing

the frame's stiffness (δ = 80 mm). A similar behaviour was noted for the case of the medium soil models. This was not the case for the soft soil models 2H30 S(A & B) that were able to maintain their stiffness and fail for a load that was 1.1 and 3.2% larger than that obtained from the fixed-base model, respectively (see Table 11). As it can be seen in Table 11, the medium soil models 2H30 M(A & B) failed for a total horizontal load of 280.32 kN that was 2.1% lower compared to the fixed-base model. The differences in the obtained maximum failure loads are attributed to the strain re-distribution due to the SSI effect that leads to a different internal stress development. It must be noted that the curves shown in Fig. 27 were developed by removing the rigid body horizontal deformation of the frame.

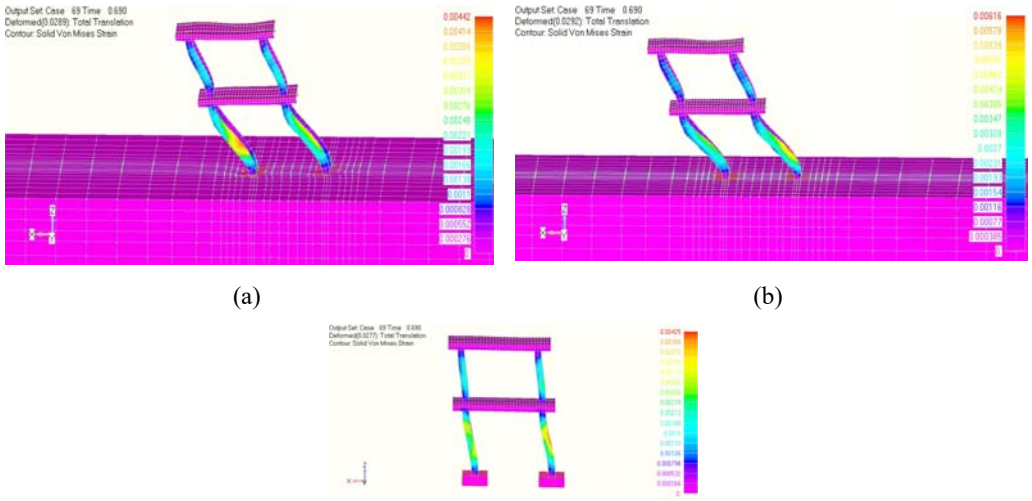

(a) (b)

(c)

Figure 28. 4-column RC frame building. Von Mises strain contours obtained from pushover analysis of models (a) 2H30 S(A), (b) 2H30 M(A) and (c) 2H30 (F).

	Base Shear Strength V (kN)	$\frac{(V_{SSI}-V_{fixed})}{\delta V_{fixed}}$ (%)
2H30 S(A)	289.36	1.1
2H30 M(A)	280.32	-2.1
2H30 S(B)	295.39	3.2
2H30 M(B)	280.32	-2.1
2H30 (F)	286.35	-

Table 11. Maximum Displacement and Base shears of the H30 frame models.

4.3 Evaluation of the Proposed Algorithm

A numerically stable and efficient nonlinear dynamic simulation of the seismic response of structures is of great importance for the safe and economic design of these structures. The highly nonlinear response of concrete during the cyclic excitation often lead to unstable solutions or to the inability to achieve convergence as well as when the opening and closing of cracks and soil material nonlinearities are accounted for.

Through this numerical investigation it was verified that the simulation approach implemented for the SSI of RC structures with different types of soil domains, can be considered to give a robust and efficient tool for the seismic design and assessment of RC structures. Fig. 30 shows the number of internal iterations per dynamic load increment for the case of the RC 4-column building fixed-base model, where it can be

observed that the dynamic response of the RC frame was retained to a minimal number of internal Newton-Raphson iterations. According to this nonlinear dynamic analysis with 567 time steps, the total number of internal iterations was 651, which constitutes an average number of internal iterations per dynamic step equal to a mere 1.15. This finding highlights the numerical stability and robustness of the developed nonlinear algorithm for solving this numerically challenging structural problem related to RC structures. The average solution time for each internal iteration was approximately 0.24 seconds through the use of a 3.7 GHz computer processing unit.

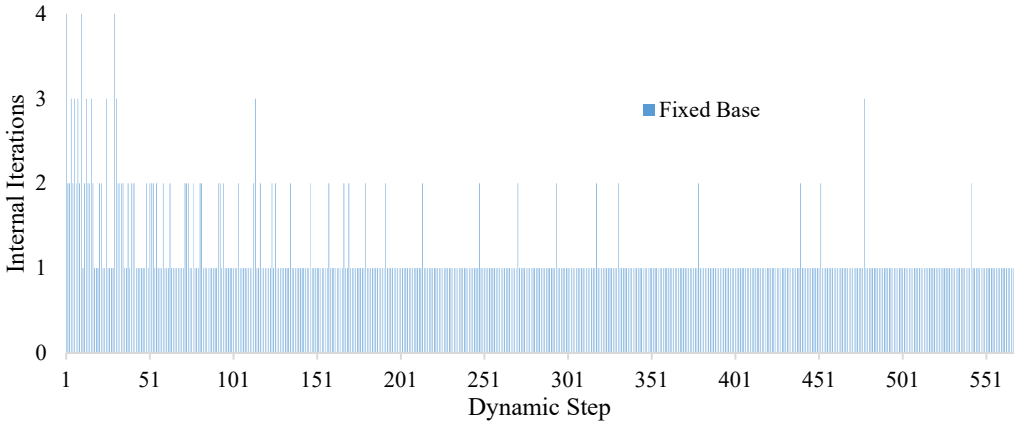

Figure 29. RC building. Number of internal iterations per dynamic load increment. Fixed-base model.

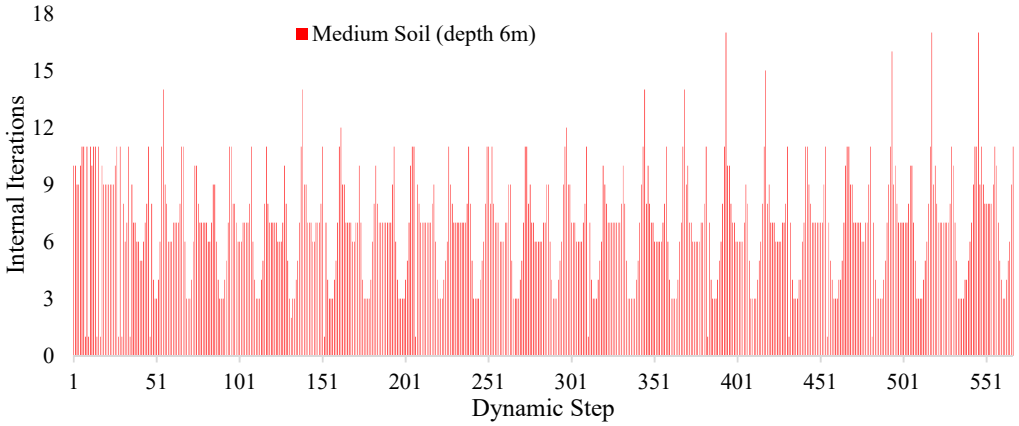

Figure 30. RC building. Number of internal iterations per dynamic load increment. 2H30 M(A) model.

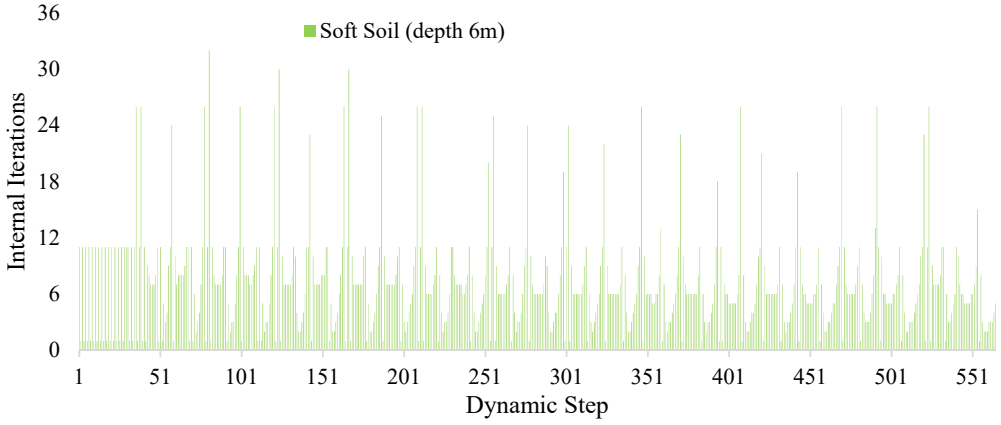

Figure 31. RC building. Number of internal iterations per dynamic load increment. 2H30 S(A) model.

Figs. 30 and 31, show the respective internal iterations per dynamic step for the 2H30 M(A) and S(A) models, respectively. It can be observed that the increase of nonlinearities due to the soil domain significantly affects the generated unbalanced forces during the nonlinear dynamic analysis of the RC frame. The average internal iterations per time step was 6.75 and 6.97 for the case of the medium and soft soil domain, respectively. As it is expected, the soft soil model derived a larger number of internal iterations compared to the model with the medium soil domain, attributed to the higher soil nonlinearities developed at the softer soil domain around the footings of the structure.

The average computational time for solving one internal Newton-Raphson iteration for the case of the 2H30 M(A) and S(A) models was around 20 seconds. Even though this is not an excessive computational time for a problem with 31,000 degrees of freedom (stiffness matrix size 400 Mb), it is time consuming when the number of time steps is more than 2,000 and the respective internal iterations close to 10,000 in total.

5. Conclusions

This study investigates the SSI phenomenon and its effect on RC frame buildings and their dynamic-seismic response under low and high in magnitude accelerations. For the material of concrete, a 3D brittle material model developed in [50], is used in order to take into account the triaxial behaviour of concrete and the effect of crack opening and crack closure during cyclic and dynamic loading conditions. The opening of cracks is treated with the smeared crack approach. For the material of soil, the Ramberg-Osgood [54] material model is used in order to take into account the deterioration of shear stiffness of the material during cyclic loading conditions. Both material models have been implemented into 3D isoparametric finite elements that were used to discretize the exact geometry of the under-study structures and soil domains.

A preliminary investigation was performed by using a two-storey RC plane frame, where it was subjected to a sine-like accelerogram adjusted based on the natural frequency of the specimen in order to achieve maximum inertia forces. The RC plane frame was assumed to be founded on hard, medium and soft soil domains, where it was concluded that the developed displacements obtained from the SSI models increased by 2-7% compared to the fixed-base model, where the predicted base shear was found to decrease by 20-30%. It was also found that the most important factor to explain the impact of the SSI during a nonlinear analysis, is the evolution of damage of the system. Furthermore, the SSI models produced larger amount of dissipated energy than the fixed-base model, while as the depth of the soil increases the dissipating mechanisms are also increased. It has to be noted that the hard soil models suffered for severe damage (cracking) and managed to develop similar amount of dissipated energy with the soft soil models. Even though the RC frame was realistic (tested in a laboratory through a shaking table experiment) it was found to be small in size, while its mass was not sufficiently large to provide with significant SSI effects.

The above mentioned RC plane frame was used to construct a 4-column RC frame that was thereafter used to investigate in depth the SSI effect under low and higher in magnitude accelerograms. The RC building was first analysed by assuming a fixed-base and then solved for a medium and soft soil domains by assuming a 6 and 11 m depths of the two different in terms of stiffness soil domains. The results indicated that the softer the soil is, the larger the derived displacements are. It was also found that the maximum displacement increase was equal to 95% for the case of the 6m deep soft soil domain. This finding is in line with the overall observations found in the international

literature, whereas the numerical investigation revealed that the deeper soil domain derived a smaller displacement increase compared to the smaller in-depth soil domain models (A). This was attributed to the fact that the flexibility of the soil can also increase the energy dissipation of the system and delay its structural failure.

Furthermore, the vertical component of displacements was investigated during the nonlinear dynamic analysis and was found that its effects on the dynamic response of the SSI models was insignificant compared to the substantial increase at the base shear. This increase is attributed most likely to the resonance phenomenon between the structure, soil domain and the imposed sine-like accelerogram.

In order to investigate the ultimate limit state of the RC building taking into consideration the SSI effect, the RC structure was analysed by applying the low accelerogram and then the higher in magnitude accelerogram consecutively through a single analysis. According to the numerical results obtained, it was found that the model with the softer soil domain developed larger displacements during the first excitation, while the model with the medium soil domain developed larger deformations and base shear that eventually led to an instability of the structure, during the second excitation. The evolution of the value of the eigen-frequency of the system shows that the SSI model suffered a smaller amount of damage than the medium soil and the fixed-base models. Additionally, most damages appeared at the fixed-base model which evidently developed the lowest base shear during the nonlinear dynamic analysis. The two SSI models predicted a frame failure with large remaining deformations due to both RC material damages at the ground floor columns and soil nonlinearities. The medium soil model though derived larger deformations that led to developing large damages earlier compared to the soft soil model. This is attributed to resonance that was caused by the stiffness change of the superstructure due to relevant damage development that led the medium soil model to develop close to 500% increased displacements compared to the fixed-base model.

The soft soil model's response, highlighted the fact that when structures are found on softer soils can delay the structural failure because of the soil's increased dissipating mechanisms and the shift of the damage locations during the nonlinear dynamic analysis. In addition, the fixed-base model was found to be able to undertake both accelerograms without the development of excessive permanent deformations. The major and sudden decrease of the stiffness of the fixed-base model at the beginning of the analysis made the system more flexible with smaller base shear development compared to the other two models, thus managed to withstand both seismic excitations without developing a failure mechanism nor large permanent deformations. This finding highlights the significant effect of the SSI phenomenon on the nonlinear dynamic response of the RC building under ultimate limit state dynamic loading. It is also safe to conclude that the softer the soil domain is, the higher the expected energy dissipation of the system is. This also can explain why the RC building did not become unstable at an earlier stage compared to the frame founded on medium soil.

Thereafter, a pushover analysis has been conducted to investigate the influence of SSI on the RC structure with 4 columns. It has to be noticed that the fixed-base model developed a sudden loss in strength when the horizontal displacement reached 80 mm, where it became more flexible than the other models, a mechanical response that eventually led to a slightly lower maximum base shear capacity compared to the soft soil model, while the medium soil model was the one that derived the lowest maximum base shear out of the 5 models that were investigated. Based on the monotonic analysis results, it was evident that the SSI effect can affect the damage distribution within the superstructure altering the plastic hinge development and therefore modify the damage

development during the nonlinear analysis, whereas alter the final failure mechanism. Even though the SSI effect was present, it was found that the ultimate capacity of the RC structure was not affected significantly (maximum deviation from the fixed-base model was 3.2%), which is a numerical finding that highlights the importance of performing nonlinear dynamic analysis if the objective is the realistic assessment of the expected seismic response of our RC structures.

Finally, future work will investigate the effect of larger in size RC frames, deriving a general rule related to the connection between the SSI effect and the fundamental frequency of the superstructure and soil domain. Different foundation systems will be included in this investigation in order to reach more concrete conclusion on this poly-parametric structural nonlinear dynamic problem.

Acknowledgment

The analysis of the developed large-scale numerical models was performed through the use of a fast PC that was purchased under the financial support received from the Research Development Programme (RDP), year 2019, round No 1, University of Pretoria, under the project titled Future of Reinforced Concrete Analysis (FU.RE.CON.AN.); a research fund awarded to the sixth author in support to his research activities. This financial support is highly acknowledged.

REFERENCES

[1] ASCE. ASCE 7-10 Minimum design loads for buildings and other structures. American Society of Civil Engineers; 2010

[2] NEHRP. NEHRP recommended provisions for seismic regulations for new buildings and other structures. Part 1: Provisions 2009 edition, FEMA 750 CD

[3] Bielak J. Earthquake response of building-foundation systems. Technical report: CaltechEERL:1971.EERL-71-04. California Institute of Technology 1971.

[4] Jennings PC, Bielak J. Dynamics of building-soil interaction. Bulletin of the Seismological Society of America 1973;63(1):9–48

[5] Veletsos AS, Meek JW. Dynamic behaviour of building-foundation systems 1974;3(2):121–38. Earthquake Engineering and Structural Dynamics 1974;3(2): 121–38.

[6] Luco JE. Linear soil structure interaction. In: Seismic Safety Margins Research Program (Phase I). US Nuclear Regulatory Commission. Washington, DC; 1980.

[7] Roesset JM. A review of soil-structure interaction. In: Soil-structure interaction: the status of current analysis methods and research. Johnson JJ, editor. Rpt. no. NUREG/CR-1780 and UCRL-53011. US Nuclear Regulatory Commission. Washington, DC, and Lawrence Lab, Livermore, CA; 1980

[8] Mylonakis G, Gazetas G. Seismic soil-structure interaction: beneficial or detrimental? Journal of Earthquake Engineering 2000;4(3):377–401.

[9] Rodriguez ME, Montes R. Seismic response and damage analysis of buildings supported on flexible soils. Earthquake Engineering and Structural Dynamics 2000;29(5):647–65

[10] Avilés J, Pérez-Rocha LE. Soil–structure interaction in yielding systems. Earthquake Engineering and Structural Dynamics 2003;32(11):1749–71.

[11] Nakhaei M, Ghannad MA. The effect of soil–structure interaction on damage index of buildings. Engineering Structures 2008;30(6):1491–9.

[12] Saez E, Lopez-Caballero F, Razavi A. Inelastic Dynamic Soil-structure Interaction Effects onMoment-resisting Frame Buildings. Engineering Structures 2013;51:166-177.

[13] Veletsos AS, Verbic B. Dynamics of elastic and yielding structure-foundation systems. In: Proceedings of the Fifth World Conference Earthquake Engineering. Rome, Italy 1973; pp. 2610–2613.

[14] Bielak J. Dynamic response of non-linear building-foundation systems. Earthquake Engineering and Structural Dynamics 1978;6:17–30.

[15] Avilés J. and Pérez-Rocha L.E., Soil-structure interaction in yielding systems, Earthquake engineering and Structural Dynamics, 2003, 32(11): 1749–1771.

[16] Zhang, J. and Tang, Y. Dimensional analysis of structures with translating and rocking foundations under near-fault ground motions, Soil Dynamics and Earthquake Engineering 2009, 29(10): 1330–1346.

[17] Moghaddasi, M., Cubrinovski, M., Chase, G.J., Pampanin, S. and Carr, A. Probabilistic evaluation of soil-foundationstructure interaction effects on seismic structural response, Earthquake Engineering and Structural Dynamics 2011, 40(2): 135-154.

[18] Jarernprasert S, Bazan-Zurita E, Bielak J. Seismic soil-structure interaction response of inelastic structures, Soil Dynamics and Earthquake Engineering 2013; 47: 132–143.

[19] Lu, Y., Hajirasouliha, I. and Marshall, A.M. "Performance-based seismic design of flexible-base multi-story buildings considering soil–structure interaction", Engineering Structures 2016;108: 90-103.

[20] Tomeo R, Bilotta A, Pitilakis D, Nigro E. Soil-structure interaction effects on theseismic performances of reinforced concrete moment resisting frames. Procedia Engineering 2017;199:230–5

[21] Sextos, A.G. and Ekonomakis, M.M. Frequency-dependent proxies of soil-structure interaction impact for typical R/C buildings. 1st International Conference on Natural Hazards & Infrastructure (ICONHIC) 28-30 June, 2016, Chania, Greece

[22] Diaz O, Mendoza E, Esteva L. Seismic ductility demands predicted by alternate models of building frames. Earthquake Spectra 1994;10:465–87.

[23] Hajirasouliha I, Doostan A. A simplified model for seismic response prediction of concentrically braced frames. Advances in Engineering Software 2010;41:497–505.

[24] Wolf, J.P. Dynamic Soil–Structure Interaction, Prentice-Hall, Englewood Cliffs, NJ, 1985.

[25] Wolf, J.P. Soil–Structure Interaction Analysis in Time Domain, Prentice-Hall, Englewood Cliffs, NJ, 1988

[26] Clough, R.W., Penzien, J. Dynamics of Structures, second ed., McGraw-Hill, Tokyo, 1993

[27] Lysmer, J., Udaka, T., Tsai, C., Seed, H.B. FLUSH: a computer program for approximate 3D dynamic analysis of soil–structure problems, Report of Earthquake Engineering Research Center, University of California, Berkeley, Report No. EERC75-30, 1975.

[28] Meek, J.W., Wolf, J.P. Cone models for homogenous soil, part I, Journal of Geotechnical Engineering 1992;118: 667-685.

[29] Meek, J.W., Wolf, J.P. Cone models for homogenous soil, part II, Journal of Geotechnical Engineering 1992;118: 686-703.

[30] Wolf, J.P., Meek, J.W. Cone models for a soil layer on a flexible rock half-space, Earthquake Engineering and Structural Dynamics 1993;22:185-193.

[31] Kausel E., Roesset J.M., Christian J.T. Non-linear behaviour in soil–structure interaction. Journal of the Geotechnical Engineering Division – ASCE 1976;102(GT12):1159–78.

[32] Lysmer J, Tabatabaie-Raissi M, Tajirian F, Vahdani S, Ostadan F. SASSI: a system for analysis of soil–structure interaction. Report no. GT-81/02, Geotechnical Engineering, University of California, Berkeley; 1981.

[33] Pitilakis D, Dietz M, Wood DM, Clouteau D, Modaressi A. Numerical simulation of dynamic soil–structure interaction in shaking table testing. Soil Dynamics and Earthquake Engineering 2008;28(6):453–67

[34] Behnamfar, F. ; Banizadeh, M.: Effects of Soil Structure Interaction on Distribution of Seismic Vulnerability in RC Structures. In: Soil Dynamics and Earthquake Engineering 2016;80:73–86.

[35] Pavlatos GD, Beskos DE. Dynamic inelastic soil–structure interaction using a hybrid BEM/FEM scheme. In: Mang, Rammerstorfer, editors. IUTAM symposium on discretization methods in structural mechanics. Kluwer; 1999. p. 233–40.

[36] Nova R, Montrasio L. Settlements of shallow foundations on sand. Géotechnique 1999;41(2):243–56

[37] Crémer C, Pecker A, Davenne L. Cyclic macro-element for soil–structure interaction: material and geometrical non-linearities. International Journal for Numerical and Analytical Methods in Geomechanics 2001;25:1257–84.

[38] Grange S, Kotronis P, Mazars J. A macro-element for a circular foundation to simulate 3D soil–structure interaction. International Journal for Numerical and Analytical Methods in Geomechanics 2008;32(10):1205–27.

[39] Pecker A, CHatzigogos T. Non linear soill structure interaction impact on the seismic response of structures. XIV European Conference on Earthquake Engineering, 2010.

[40] Menglin L, Huaifeng CX, Yongmei Z. Structure–soil–structure interaction: literature review. Soil Dynamics and Earthquake Engineering 2011;31:1724–31.

[41] Celebi E, Göktepe F, Karahan N. Non-linear fnite element analysis for prediction of seismic response of buildings considering soil-structure interaction. Natural Hazards and Earth System Science 2012;12:3495–505.

[42] Hussien MN, Karray M, Tobita T, Iai S. Kinematic and inertial forces in pile foundations under seismic loading. Computers and Geotechnics 2015;69:166–81.

[43] Hokmabadi AS, Fatahi B, Samali B. Assessment of soil–pile–structure interaction influencing seismic response of mid-rise buildings sitting on floating pile foundations. Computers and Geotechnics 2014;55:172–86

[44] Torabi H, Rayhani MT. Three dimensional Finite Element modeling of seismic soil–structure interaction in soft soil. Computers and Geotechnics 2014;60:9–19.

[45] Amorosi A, Boldini D, di Lernia A. Dynamic soil-structure interaction: a three-dimensional numerical approach and its application to the Lotung case study. Computers and Geotechnics 2017;90:34–55.

[46] de Silva F, Pitilakis D, Ceroni F, Sica S, Silvestri F. Experimental and numerical dynamic identifcation of a historic masonry bell tower accounting for different types of interaction. Soil Dynamics Earthquake Engineering 2018;109:235–50.

[47] López Jiménez GA, Dias D, Jenck O. Effect of the soil–pile–structure interaction in seismic analysis: case of liquefable soils. Acta Geotechica 2018:1–17

[48] Markou G., Papadrakakis M., Computationally efficient 3D finite element modeling of RC structures. Computers and Structures 2013;12(4), 443–98.

[49] Mourlas, C., Papadrakakis, M., Markou, G. A computationally efficient model for the cyclic behaviour of reinforced concrete structural members. Engineering Structures 2017;141: 97–125.

[50] Mourlas, C., Markou, G. and Papadrakakis, M. Accurate and computationally efficient nonlinear static and dynamic analysis of reinforced concrete structures considering damage factors. Engineering Structures 2019;178: 258–285.

[51] Markou, G., Mourlas, C., Bark, H. and Papadrakakis, M. Simplified HYMOD non-linear simulations of a full-scale multistory retrofitted RC structure that undergoes multiple cyclic excitations – An infill RC wall retrofitting study. Engineering Structures 2018;176: 892–916.

[52] Markou, G., Sabouni, R., Suleiman, F. and El-Chouli, R. Full-Scale Modeling of the Soil-Structure Interaction Problem Through the use of Hybrid Models (HYMOD). International Journal of Current Engineering and Technology 2015;5(2): 885-892.

[53] Kotsovos, M.D., "Finite-Element Modelling of Structural Concrete: Short-Term Static and Dynamic Loading Conditions", CRC Press, 2015.

[54] Ramberg, Walter; Osgood, William R.: Description of Stress-Strain Curves by There Parameters / National Advisory Committee for Aeronautics. Washington, July 1943. – Research Report

[55] Martakis, P., Taeseri, D., Chatzi, E., & Laue, J. A centrifuge-based experimental verification of Soil-Structure Interaction effects. Soil Dynamics and Earthquake Engineering 2017;103:1-14

[56] Carydis P., "Shaking table tests of R.C. frames, ECOEST PPREC8", 1997, Report 8, 182.

[57] Willam K. J. and Warnke E. P., "Constitutive model for the triaxial behaviour of concrete", Seminar on concrete structures subjected to triaxial stresses, Instituto Sperimentale Modeli e Strutture, Bergamo, Paper III-1, 1974.

[58] Menegotto, M., and Pinto, P. E. Method of analysis for cyclically loaded reinforced concrete plane frames including changes in geometry and non-elastic behaviour of elements under combined normal force and bending. Proceedings, IABSE Symposium on Resistance and Ultimate Deformability of Structures Acted on by Well Defined Repeated Loads, Lisbon, Portugal, 1973,15–22.

[59] Masing, G.: Eigenspannungen und Verfertigung beim Messing. Zurich, 1926. – 2nd International Congress on Applied Mechanics

[60] AlHamaydeh, M., Markou, G. and Saadi, D., Nonlinear FEA of Soil-Structure-Interaction Effects on RC Shear Wall Structures, 6th International Conference on Computational Methods in Structural Dynamics and Earthquake Engineering, 15-17 June 2017, Rhodes Island, Greece.

[61] Reconan FEA v2.0, User's Manual, 2020.

[62] Gravett, D.Z. and Markou, G., State-of-the-Art Investigation of Wind Turbine Structures Founded on Soft Clay by Considering the Soil-Foundation-Structure Interaction Phenomenon – Optimization of Battered RC Piles, Under Review.

[63] Knappett, J. and Craig, R. F. Craig's Soil Mechanics, Eighth Edition. Taylor & Francis, 2012.

[64] Carter, M. and Bentley, S.P., Correlations of Soil Properties, Pentech Press, London, 1991.

[65] K.-J. Bathe, Finite element procedures. Prentice Hall Engineering, Science, Mathematics, New York: Prentice Hall, 1996.

[66] CEN. Eurocode 8: Design of structures for earthquake resistance. Part 1: general rules, seismic actions and rules for buildings. European Standard EN 1998-1:2004, Comite Européen de Normalisation, Brussels, Belgium, 2004.

[67] Hussein A. Bark, Implementation of a Nonlinear Soil Material Model into a FEA Framework for the Simulation of the Seismic Soil-Structure Interaction, master thesis, Technical University Munich, 2019.